CODEN:LUTEDX/(TEIE-5525)/1-107/(2025)

Industrial Electrical Engineering and Automation

Development of a Mechanical Image Stabilization Method to Counter-act Rotational Disturbances

Oskar Karlsson

Division of Industrial Electrical Engineering and Automation
Faculty of Engineering, Lund University

Master Thesis

Development of a Mechanical Image Stabilization Method to Counter-act Rotational Disturbances

by:

Oskar Karlsson

Division for Industrial Electrical Engineering and Automation,
Faculty of Engineering,
Lunds Tekniska Högskola

LUND
UNIVERSITY

Abstract

Image stabilization is critical in producing usable footage recorded by Body-worn Cameras, which are subject to external disturbances caused by biomechanical factors, such as body movement while walking and running. The thesis work is carried out by first defining the nature of the disturbances upon which stabilization techniques are investigated, by reviewing literature and by gathering data using image analysis and sensor information. An active system is designed and prototyped, utilizing sensors and an actuator, controlled by a micro-controller. This system is designed to reduce the disturbances caused by the rotational movement of the upper torso. The work includes selection of an actuator system and the necessary control system components and sensors, a software implementation and mechanical design. After the active system is implemented, design and testing of a passive system is done. This passive system was initially thought to dampen the disturbances due to reciprocating motion of the camera housing, but the difference was negligible. The passive system does however provide support for the camera housing by providing a firm attachment between the camera and mounting solution, thus reducing disturbances. Lastly, an alternative to the actuator used in the active system is explored. This actuator conceptualization is supported by simulations and calculations, providing a foundation for a new actuator. This thesis provides methods for stabilizing a body-worn camera with accompanying methods for evaluating efficiency of methods. Active, passive, and combined image stabilization systems have been compared to a system without stabilization and the results are as follows: The largest increase in horizontal stability is achieved by employing an active system, reducing the horizontal displacement of the video feed by 69.5%. The largest increase in vertical stability is achieved by a passive damping mechanism, reducing the vertical displacement of the video feed by 15%. Combining the two and using a stiff damping material results in a 66% reduction in displacement horizontally, and 44.5% reduction in vertical displacement.

Keywords: Mechanical Image Stabilization, Body-worn Camera, Actuator, Image Analysis

List of Abbreviations

MIS: Mechanical Image Stabilization
EIS: Electronic Image Stabilization
OIS: Optical Image Stabilization
AS: Active Stabilization
PS: Passive Image Stabilization
IMU: Inertial Measurement Unit
PID: Proportional-Integral-Derivative (Control)
VCA: Voice Coil Actuator
BLDC(M): Brushless Direct Current (Motor)
DOF: Degree of Freedom
ISLA: Image Sensor and Lens Assembly
PWM: Pulse Width Modulation
SVM: Space Vector Modulation
FSM: Finite State Machine
CAD: Computer Aided Design

Acknowledgements

I would like to thank my academic supervisor at IEA, Avo Reinap, for his insights and helpful discussions throughout this thesis. I would also like to thank my company supervisor, Erik Gustafsson, and all other colleagues at SPM and SPE for support and practical help.

Preface

The thesis work was carried out at an external company, backed by the Division of Industrial Electrical Engineering and Automation (IEA) at LTH. The sole contributor to the content of this thesis is Oskar Karlsson.

Contents

Chapter 1

Introduction

1.1 Background

Body worn cameras are cameras used widely both in professional contexts, such as law enforcement and security but also hobby or journalism contexts, as in Figure 1.1 [1], where people want to capture footage in first-person-perspective. As body worn cameras are used in dynamic environments, the quality of recorded footage depends on the movement of the operators' body – a biomechanical[1] factor. In environments where the operator is sprinting, the camera produces footage that is highly different from what is recorded during i.e. walking. The footage has issues of being shaky and unstable, making it hard to review it and the value of the footage decreases the more disturbances there are. There are ways to mitigate the effects of these disturbances, such as stabilizing the footage both in real time and during post-processing using software. This is called Electronic Image Stabilization (EIS), and is today used in a lot of camera products. The issue with stabilization based on software is that it stabilizes the image at the cost of quality and resolution, as it works by cropping each frame by utilizing a portion of the frame as a buffer for motion which ultimately leads to a smaller resolution of the recorded footage. In environments where the camera is static and overlooking the same position or working on a rotation of multiple static positions, this is usually enough to produce stable recordings. These recordings are then be reliable and useful in a context of security.

EIS is rather simple to implement, but limited in the range of compensation it can provide. Therefore, the next step is to explore Mechanical Image Stabilization (MIS) to reduce the amount of the image that the EIS crops. The main concern is that of rotational disturbances, back and forth movement around the axis of rotation, exerted on the camera housing, and by extension the Image Sensor and Lens Assembly, abbreviated as ISLA in

[1] the mechanics of biological and especially muscular activity (as in locomotion or exercise) [2]

Figure 1.1: Example usage of bodycam: A reporter live-streaming with the use of a GoPro Hero2. [1]

this thesis, resulting in too large disturbances to be handled by EIS. Today, there is a system concept developed to do this but it is not implemented in the actual product due to needing further investigation. The added weight of the system adds the necessity of a more efficient MIS system, and reducing size and weight is beneficial in both cost and efficiency.

1.2 Scope

The scope of this Master's thesis is to evaluate what methods can be used to reduce disturbances or even stabilize footage. Firstly, a suitable system must be investigated and developed. Combinations of stabilization techniques, such as active and passive MIS are compared, analysed and reported in this thesis. Control methods and implementation are reviewed and a prototype is constructed, which uses conventional electric motors. Following this is a conceptualization of an alternative actuator. As a final step, the system is developed and compared to similar systems.

1.3 Problem Formulation

This thesis aims to define the disturbances exerted on the Body-worn Cameras (BWC) and investigate what methods can be used to reduce these disturbances, in order to stabilize the recorded footage. Stabilization is required for the ISLA and the camera body. This requires review of previous work related to stabilization of the BWC [3][4], but also gathering of information regarding stabilization methods in general. The literature review's purpose is to construct a solid foundation for developing a system to stabilize the camera by exploring methods to measure disturbances, established methods for stabilization and what type of components might be needed.

The disturbances exerted on the camera have the characteristics of high amplitude and low frequency, effectively generating a large deviation in the direction of which the camera module is aimed. Other disturbances that can affect the cameras stability are investigated and analyzed. These disturbances are sought to be reduced through this thesis. Previous work [3][4] has been done regarding this issue, which aids in gaining an understanding for the underlying issues and which methods have been explored previously.

In order to generate viable concepts, it is important to identify and understand what the cause of the disturbances are, how the problem has been approached before and if there are any new types of approaches to be made. This is done through thorough research of earlier works such as Bryngelsson and Gustafsson [3] and Bladh and Göransson [4], as well as data analysis and using a structured product development method.

- What characterizes the disturbances affecting the recorded footage?
- What mechanical, electro-mechanical or combined methods can be used to reduce these disturbances?
- Will the proposed system be scalable?

1.4 Previous Findings

In their respective Master thesis', Bladh and Göransson, and Bryngelsson and Gustafsson conclude early on in their thesis that the translational motion, i.e. the motion in vertical up-down direction, is not of main concern [3] [4]. They choose to focus on the rotational motion that occurs around the vertical axis and one of the horizontal axes, which are further described in Chapter 2. While it may be true that the rotational motion affects the footage the most, there might be indirect solutions to this from studying ways to reduce the vertical translational motion.

- It was concluded that wearing a harness mount is the best option for stabilizing the footage mechanically [3]. To provide the best possible conditions for evaluating the cameras performance, this mounting solution is used in this work. No other consideration is taken as to how the mounting solution affects the stability of the footage.

- A suggestion for further development is to introduce a third rotational axis in the gimbal[2] system [4]. With the current limitations of commercially available DC motors, this increases the weight. Furthermore, a third axis is not necessarily going to make the footage more stable and could possibly be handled by EIS.

- In their evaluation of the test performance, Bladh and Göransson state that the sudden change in direction and velocity when the feet hit the ground while running affects the performance of pitch compensation [4]. It is within this thesis scope to investigate if it is possible to mitigate this effect using other methods than using electronically controlled actuators.

- Controlling the yaw-angle of the ISLA is still necessary and from the results in Bladh and Göranssons work, this angle is more responsive in DC-motor compensation [4]

- Although the size of the stabilization solution is of importance, during prototyping it won't be a limiting factor. The objective here is to create a solution which can be scaled down using other or custom-made components, but this requires further research regarding voltage and current usage, and results in a too broad scope to include in this work.

- The chosen development methodology is based on selected experiments to evaluate the effectiveness of mechanical stabilization, such as active, passive and combined components.

Having identified these findings, this thesis investigates what more can be done to reduce the disturbances. This investigation has the approach of developing concepts, evaluating concepts and prototyping, following the method described by Karl T. Ulrich and Steven D. Eppinger in Product Design and Development [6].

[2] a device that permits a body to incline freely in any direction or suspends it so that it will remain level when its support is tipped [5]

1.5 Thesis Outline

The structure of this thesis is outlined below.

Chapter 1: This chapter focuses on presenting the subject of this thesis, with emphasis on providing context and giving an overview of what is sought to be achieved.

Chapter 2: This chapter provides the theoretical foundation upon which this thesis is built.

Chapter 3: In this chapter, the objective is to construct an active system that controls the direction in which the ISLA is facing.

Chapter 4: This chapter describes the process of testing, evaluating and reiterating the design of a damping system based upon materials.

Chapter 5: This chapter's purpose is to explore alternative actuator concepts.

Chapter 6: This chapter discusses the findings of the thesis.

Chapter 7: Conclusions and suggestions going further are stated here.

Chapter 2

Background and Theory

Image stabilization is an issue that primarily affects anyone needing to review footage recorded by cameras used in highly dynamic environments. This footage is often shaky and blurry, and sometimes the results are unusable. There are several techniques that are used today, namely Optical Image Stabilization (OIS), Electronic Image Stabilization (EIS) and Mechanical Image Stabilization (MIS), and they all have their advantages and disadvantages. In Figure 2.1, the multiple methods for image stabilization is shown. As can be seen, there are two main types of stabilization: Real-time and Post-processing. Essentially what this means is that EIS can be used both in real-time but also as a post-processing function with the purpose of reducing interferences in the footage. The choice of having real-time or post-processing EIS can be a choice based on processing power and power consumption of the device used. Although EIS is a common method for stabilization, due to its method of stabilization it is not possible to use in a context where large angle differences occur, and Mechanical Image Stabilization is necessary to eliminate disturbances with a larger range of angles, which is investigated in this work.

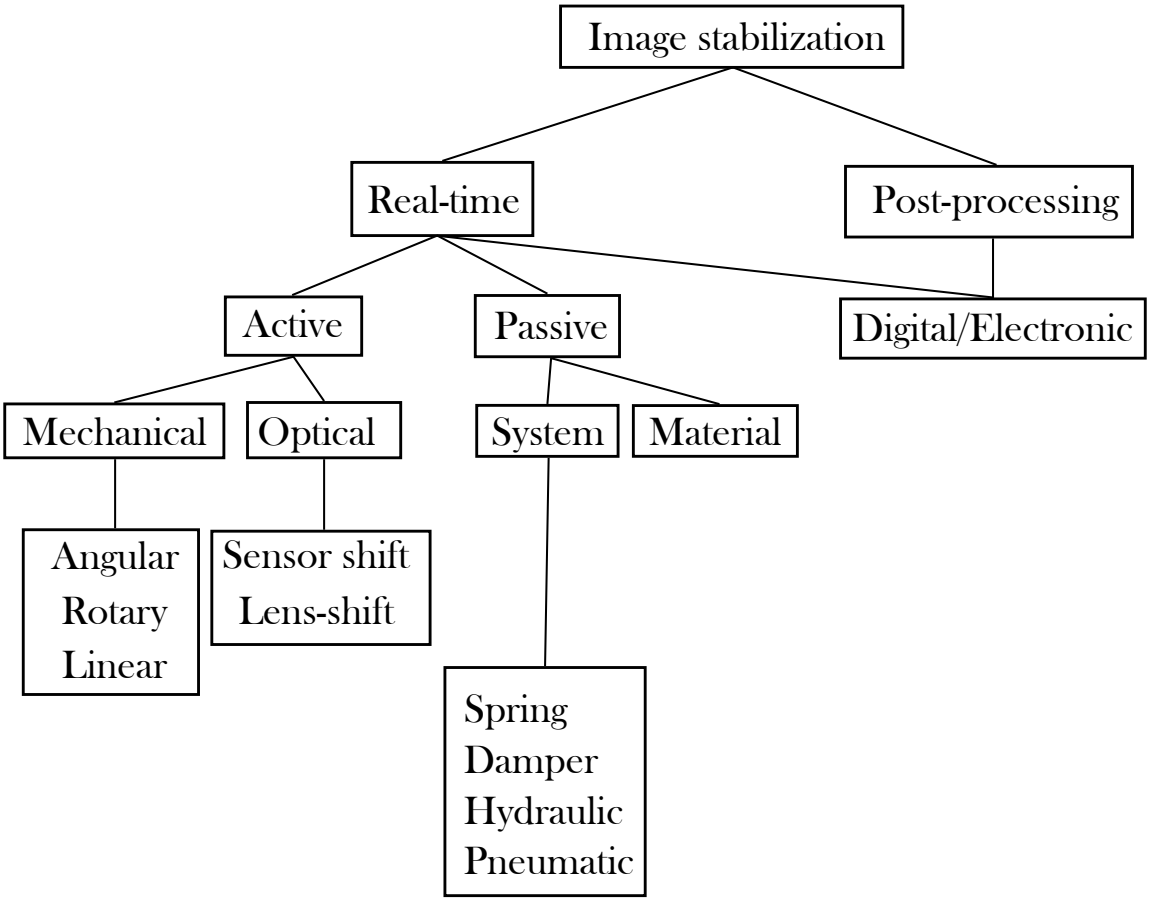

Figure 2.1: The various techniques and sub-systems for Image Stabilization.

2.1 Background

Stability

Stability[1] in the context of this thesis is the control of movement of bodies when external forces are exerted on them. In a broader sense, stability is sought after in many different areas and industries such as naval and aviation. In terms of naval stability, consider a ship on a stormy sea traveling orthogonal to the waves. The waves crash into the side of the vessel, causing it to sway back and forth along the roll axis, as described in Figure 2.2 [8]. To combat this, engineers have conceived a multitude of solutions such as electromechanical stabilizer fins, which utilize a lift-force based on gyroscope measurements, and more simple constructions such as bilge keels which are purely mechanical fins [9]. No matter what method is employed, the various stabilization systems offer increased stability of the vessel.

[1]The property of a body that causes it when disturbed from a condition of equilibrium or steady motion to develop forces or moments that restore the original condition [7]

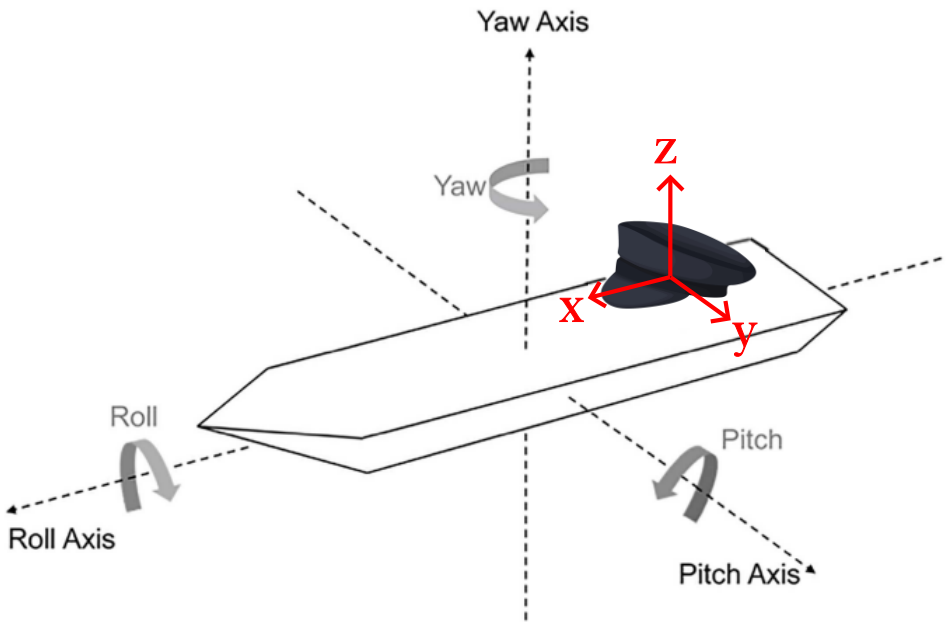

Figure 2.2: The rotational axes of a boat [8].

Biomechanics

Stability in biomechanics is not that different from the cases discussed in the previous section. Take, for example, a chickens head [10]. When held in the hands of a person who moves its' body around in any direction, the chickens head is largely unaffected by these movements and maintains a steady gaze. This is thought to be because of the neck structure of chickens as being an efficient vibration isolator.

What affects the stability of a human when moving? The exact pattern in which a human walks is different for each person but in a broader sense, the pattern is more or less the same. The lower body movement has an effect on the upper body movement, and the pendulum-like movement of the arms of course impacts the movement of the upper body as well. These effects are increased when a person is running. Consider Figure 2.3 [11], where the variation in the center of mass (COM) is shown, S is the step length and an interval COM_{max}-COM_{min} is shown. As can be seen, the center of mass varies within one gait cycle and so do the forces associated with moving. All of this affects a persons field of view and when walking it is not that noticeable. But when running, each impact the foot has with the ground distorts the gaze for a brief moment, causing instability in vision due to the rapid change in vertical movement direction. A parallel can be drawn to a camera held in one hand by a person running, where the rapid changes in direction of vertical movement will impact the frames captured. This can be an interesting area of study using gyroscope sensors to construct datasets of the effect of the foot-to-ground impact on the

human body.

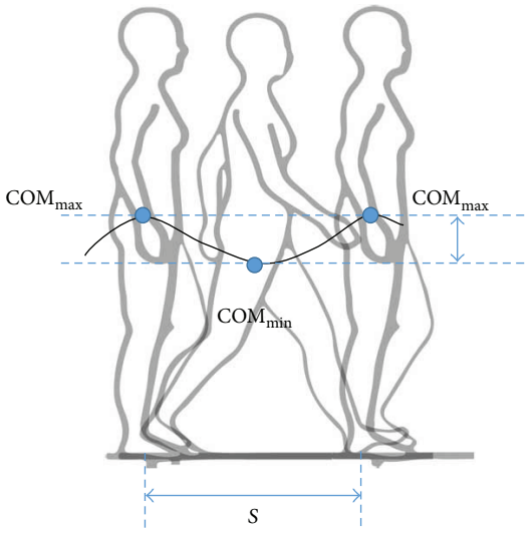

Figure 2.3: One gait cycle [11]

Fastening method

The camera fastening solution used is a harness with a back-plate that is placed on the chest, shown in Fig. 2.4 and Fig. 2.5. The normal is shown in Fig. 2.4 to illustrate the direction in which the camera (and back-plate) is facing when attached on the wearers body. When fastened, the camera used has a small gap between the protrusion on the back-plate and the back of the attached camera, allowing for some movement. What this means is that the camera is affected by vibrations and disturbances due to the variation in movement when operating in dynamic environments. This is also a contributing factor to shaky and blurry footage.

Considering now that the backplate is the part closest to the body when worn, anything that protrudes outward is more susceptible to rotational motion induced by walking and running. The camera experiences rotations about the defined axes, as in Fig. 2.2. For the problem at hand the roll is of a smaller magnitude while yaw and pitch are larger, but the main issue is to be able to reduce these rotations to produce more stable footage.

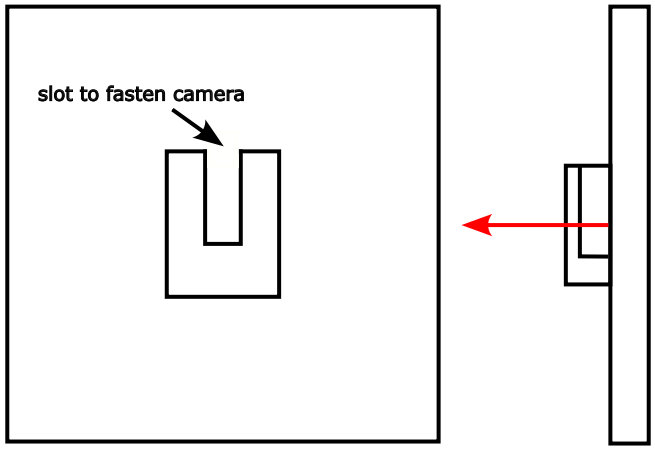

Figure 2.4: Left: Backplate shown from the front. Right: Backplate shown from the side, with its' normal shown.

Figure 2.5: The actual backplate used in the thesis.

2.2 Image Stabilization

Active Stabilization

Active Stabilization (AS) utilizes electro-mechanical components to counter-act disturbances, whether it be rotary or linear actuators, and are used in a wide variety of applications. Regarding cameras, a common type of active stabilization is a gimbal mount which stabilizes the direction at which the camera is pointing by utilizing electric actuators and sensors.

Passive Stabilization

Passive Stabilization (PS) utilizes mechanical components in order to mitigate the impact exerted by for example downwards forces. The way in which it works is to decelerate an object by in steps reducing the impact velocity. This type of stabilization is widely used in structural and industrial applications to reduce the vibrations caused by heavy machinery.

Optical Image Stabilization

Optical Image Stabilization (OIS) is a stabilization technique that uses micro-electronic components to shift the position of either the lens, or the sensor. Movements exerted on the camera by the user can be compensated for by realigning the path between the lens and sensor [12].

While OIS systems can be made compact and precise, one of the main drawbacks is that it suffers from a small dynamic range. The largest angles todays OIS systems are able to compensate are in the ranges of 1 to -1 degrees [13].

Electronic Image Stabilization

Electronic Image Stabilization (EIS) is a type of image stabilization that is entirely performed by analysing sensor information and processing the footage by software [14]. This type of stabilization has the advantage of being firmware dependent instead of hardware dependent meaning that no added components, assuming there already is a gyroscope or accelerometer in the product, are needed. It compensates well for low amplitude, high frequency oscillations in image. The principle upon which it functions is that it detects the vibrations using, often gyroscopic, data to detect of the angles in the direction the camera is facing. These oscillations typically occur because of trembling in the hands of the operator and wind. EIS performs well for cameras that are firmly mounted or used in static situations, where a low amount external movement is imposed on the camera.

Mechanical Image Stabilization

Mechanical Image Stabilization (MIS) techniques have the advantage of being able to control larger deviations of the camera angle thus minimizing the amount of footage that needs to be cropped with post-processing methods such as EIS.

Common methods of mechanical image stabilization include gimbals, which stabilizes either the camera module or the full camera housing by utilizing motorized mounts. These motors compensate for deviations in angles, based on inputs received from sensors that

detect these deviations. However, without constructing application specific motors and controllers, these solutions tend to become large in size. The added size and weight can introduce additional disturbances, depending on the original weight of the object seeking to be stabilized.

2.3 Orientation in 3D-space

No matter the technique used to stabilize a camera, it is important to clearly define the orientation within three-dimensional space in order to apply appropriate solutions to reduce disturbances. In Figure 2.6, an arbitrary object and its' coordinate system is displayed. The directions of which the coordinates axes' point is positive, and the dashed lines represent being inside the object. This is the orientation which is used throughout this thesis. When the front points towards the viewer, a two-dimensional plane is formed by the y-axis and z-axis. When the top points towards the viewer, the plane is instead formed by the x-, and y-axes. Finally, when viewing the object from the side, the plane is formed by the z-, and x-axes.

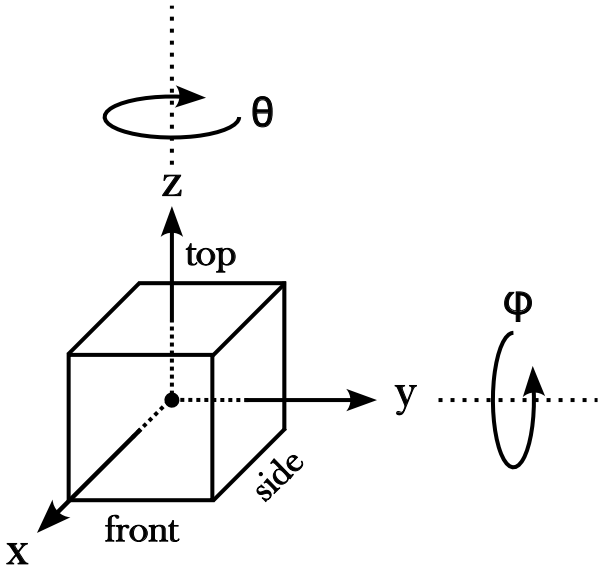

Figure 2.6: An object and its' coordinate system.

To generalize this orientation mapping, this coordinate system applies globally. What this means is that each other object in the defined three-dimensional space can be related to the global coordinate system. Mathematically, this coordinate system is described by a

vector $\overline{v}$, an identity matrix $\tilde{A}$ and the coordinate vector.

$$\begin{bmatrix} v_1 \\ v_2 \\ v_3 \end{bmatrix} = \begin{bmatrix} 1 & 0 & 0 \\ 0 & 1 & 0 \\ 0 & 0 & 1 \end{bmatrix} \begin{bmatrix} x \\ y \\ z \end{bmatrix} \tag{2.1}$$

As can be seen, from multiplying the matrix with the coordinate vector, we simply obtain the coordinate vector. Henceforth, the coordinate vector is the basis for the global coordinate system.

Any rotation exerted on the system can be described by manipulation of v with the use of rotation matrices $\tilde{R}_i$, where i = x, y, z describes which axis the object is rotated around. In Figure 2.3, the object is viewed from the top, i.e. the z-axis is pointed directly out of the paper. A counter-clockwise rotation θ around the z-axis results in the system $x' - y' - z'$ where (') notes that the axis direction has changed by θ. This rotation can be described mathematically, as seen in Eq. 2.2 and 2.3.

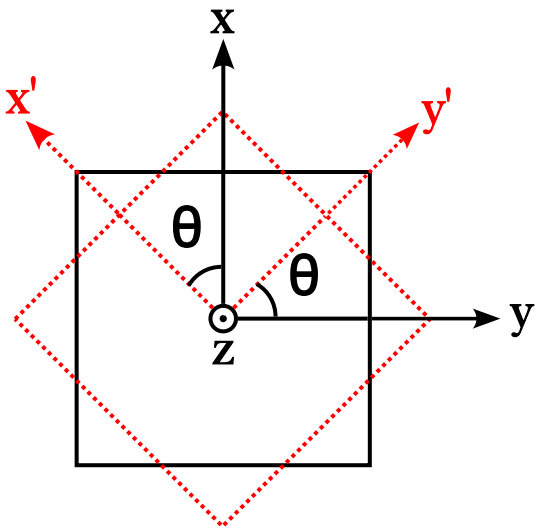

Figure 2.7: A rotation θ about the z-axis.

$$\overline{v}' = \begin{bmatrix} x' \\ y' \\ z' \end{bmatrix} = \tilde{R}_z \overline{v} = \begin{bmatrix} cos(\theta) & -sin(\theta) & 0 \\ sin(\theta) & cos(\theta) & 0 \\ 0 & 0 & 1 \end{bmatrix} \begin{bmatrix} x \\ y \\ z \end{bmatrix} \tag{2.2}$$

As can be seen from both Equation 2.2 and Figure 2.7, $z' = z$ while the other terms are described in Equation 2.3:

$$\begin{bmatrix} x' \\ y' \\ z' \end{bmatrix} = \begin{bmatrix} cos(\theta)x - sin(\theta)y \\ sin(\theta)x + cos(\theta)y \\ z \end{bmatrix} \tag{2.3}$$

The same logic applies to sequences of rotations around the other axes, but the matrices for x and y are different:

$$\tilde{R_x} = \begin{bmatrix} 1 & 0 & 0 \\ 0 & cos(\theta) & -sin(\theta) \\ 0 & sin(\theta) & cos(\theta) \end{bmatrix} \tilde{R_y} = \begin{bmatrix} cos(\theta) & 0 & sin(\theta) \\ 0 & 1 & 0 \\ -sin(\theta) & 0 & cos(\theta) \end{bmatrix}, \tag{2.4}$$

The angles considered throughout this thesis is about the z-axis, described as yaw (θ), and about the y-axis, described as pitch (ϕ) according to Figure 2.6.

Methods for calculating orientation based on measured sensor data include quaternions and Tait-Bryan angles, both of which are described in the coming sections. Regarding the active system, the angle that needs to be controlled by the active system is θ and for the passive system, the rotation about the y-axis, ϕ.

If the angle θ shown in Figure 2.7 is the angle that the body rotates, then the active system should be able to compensate for it and make it so that the system doesn't experience the full change of θ and only part of it. The ideal case is that the system completely counter-acts the change in theta, that is the desired function of the control system is to minimize the angular displacement, as described in Figure 2.8

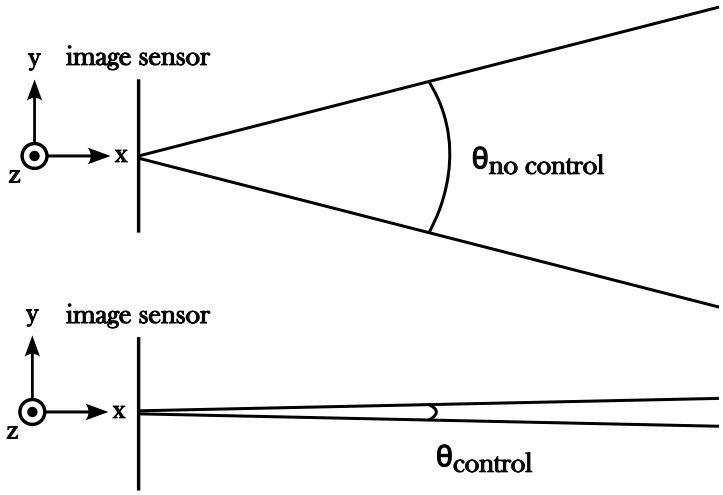

Figure 2.8: The desired output of a control system, compared to a system without control.

Tait-Bryan Angles

The Tait-Bryan angles are often described as a sequence of rotations in the frame of an aircraft. Roll is a rotation about the axis drawn from the tail to nose of the aircraft, pitch is a rotation about the axis parallel to the wings of the aircraft and yaw is a rotation about the axis drawn from the bottom of the aircraft to the top. In the context of Figure

2.4, the rotations are as follows: roll corresponds to a rotation about the x-axis, pitch a rotation about the y-axis and yaw a rotation about the z-axis [15].

Quaternions

Quaternions is a method commonly applied when calculating angles of rotation in three-dimensional space and commonly used in computer graphics [16] and robotics [17] and are often used in combination with other methods, such as Tait-Bryan angles or rotation matrices. The reason that quaternions are preferred to Euler angles is that it avoids gimbal lock, which is the loss of one degree of freedom due to two of an objects three axes becoming parallel. In navigation, the solution comes from using digital sensors, namely Inertial Measurement Units (IMU), to calculate orientation by utilizing quaternions which can then be converted into Tait-Bryan angles.

Quaternions are an extension of the imaginary numbers, containing one real component and three imaginary components:

$$q = q_r + q_x\overline{i} + q_y\overline{j} + q_z\overline{k} \tag{2.5}$$

The quaternion in Eq. 2.5 has the fundamental property, as described in [15]:

$$i^2 = j^2 = k^2 = ijk = -1 \tag{2.6}$$

To simplify readability and calculations, a quaternion can be described by the vector $\overline{q}$:

$$\overline{q} = \begin{bmatrix} q_r \\ q_x \\ q_y \\ q_z \end{bmatrix} = \begin{bmatrix} q_r \\ \overline{q_i} \end{bmatrix}, \quad \overline{q_i} = \begin{bmatrix} q_x & q_y & q_z \end{bmatrix}^T \tag{2.7}$$

If $\overline{q}$ is a unit quaternion, meaning $|\overline{q}| = \sqrt{q_r^2 + q_x^2 + q_y^2 + q_z^2} = 1$ and if its' conjugate is defined as $\overline{q}^* = [q_r - \overline{q}_i]^T$, it results in being able to represent the rotation of a vector $\overline{x}$ from the domain Ω to Ω' as $\overline{x}_{\Omega'} = q_\Omega^{\Omega'} \cdot \overline{x}_\Omega \cdot q_\Omega^{\Omega'*}$. [15] The resulting rotation matrix $R_\Omega^{\Omega'}$ is as follows:

$$R_\Omega^{\Omega'} = \begin{bmatrix} q_r^2 + q_x^2 - q_y^2 - q_z^2 & -2q_rq_z + 2q_xq_y & 2q_rq_y + 2q_xq_z \\ 2q_rq_z + 2q_xq_y & q_r^2 - q_x^2 + q_y^2 - q_z^2 & -2q_rq_x + 2q_yq_z \\ -2q_rq_y + 2q_xq_z & 2q_rq_x + 2q_yq_z & q_r^2 - q_x^2 - q_y^2 + q_z^2 \end{bmatrix} \tag{2.8}$$

A quaternion can be related to a rotation or sequence of rotations by the following set

of equations, where γ_0 is the rotational angle and $\gamma_{x,y,z}$ is the angle between the rotational axis and the x, y and z-axis respectively [18]:

$$\begin{cases} q_r = cos(\frac{\gamma_0}{2}) \\ q_x = sin(\frac{\gamma_0}{2})cos(\gamma_x) \\ q_y = sin(\frac{\gamma_0}{2})cos(\gamma_y) \\ q_z = sin(\frac{\gamma_0}{2})cos(\gamma_z) \end{cases} \tag{2.9}$$

Do note that it is only half the angle due to q and -q represents the same rotation. This is accounted for when converting back to Tait-Bryan angles. A rotation purely around the x-axis results in:

$$\overline{q} = \begin{bmatrix} cos(\frac{\gamma_0}{2}) \\ sin(\frac{\gamma_0}{2})cos(0°) \\ sin(\frac{\gamma_0}{2})cos(90°) \\ sin(\frac{\gamma_0}{2})cos(90°) \end{bmatrix} = \begin{bmatrix} cos(\frac{\gamma_0}{2}) \\ sin(\frac{\gamma_0}{2}) \\ 0 \\ 0 \end{bmatrix} \tag{2.10}$$

This allows for ease of conversion between quaternions and Tait-Bryan angles, as follows [19]:

$$\begin{cases} q_r = cos(\frac{\gamma_0}{2}) \\ q_x = sin(\frac{\gamma_0}{2}) \end{cases} \iff \frac{q_x}{q_r} = tan(\frac{\gamma_0}{2}) \iff \gamma_0 = 2tan^{-1}(\frac{q_x}{q_r}) \tag{2.11}$$

2.4 Shock & Vibration Absorption

Shock absorption and vibration absorption is a common topic in civil engineering and the automotive industry, but can also be applied to dampening of small electrical machinery, such as drones and RC cars. Shock and vibration absorption can be separated into two types; active and passive, with certain systems being hybrids, i.e. utilizing both active and passive elements [20]. Passive components include materials, spring isolators, airbags, rubber isolators etc. for applications such as attenuating structural vibrations and reducing the shaking of mechanical machinery.

Active vibration absorption utilize passive components coupled with actuators, such as linear or rotary devices, complete with a control system [20]. This type of absorption is used in industries such as automotive, aviation and marine to reduce the vibrations induced by road conditions, turbulence and engines.

The advantages of passive shock and vibration absorption is that it doesn't require

powering from a battery, while its' function is to consume vibrational energy. If tuned correctly, a passive system can attenuate vibrations exerted on the system. However, it will not be a suitable option in every dynamic environment where the disturbances vary, but it is deemed suitable in the context of this thesis. Here, active systems perform better with the cost of being energy consuming and utilizing electronic components which complicate the construction and applicability in smaller equipment [21]. Furthermore, the choice of absorption system also depends on the range of frequency needed to be attenuated. It has been proven certain passive dampening components are able to adequately attenuate low frequencies given the setup is appropriately tuned [21]. Consider Figure 2.3 where the COM_{max} completes one period for each step length, S. The frequency of one gait cycle can then be described as $f = \frac{1}{S}$

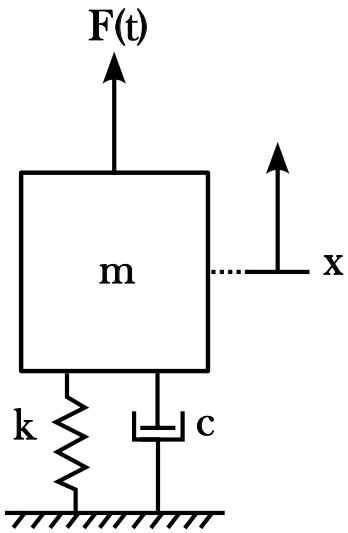

Figure 2.9: A simple mass-damper system.

Consider the single-axis linear motion in Figure 2.9, with displacement x, an applied time-varying force F(t), stiffness coefficient k [N/m] and viscous damping coefficient c [Ns/m]. Here, the components shown as a spring and a damper are arbitrary representations for a damping system, and whether it is a shock absorber, an actual spring and damper, a material etc. is irrelevant as the case applies to all of the aforementioned systems. Important to note for the system is that the "ground" plane that's drawn is in the use case the back plate shown in Figure 2.5. This means that the ground plane itself is also moving, which is not considered in Figure 2.9.

Replacing the spring and damper with the forces they exert on the object results in figure 2.10. Newton's second law of motion describes a system as the sum of forces on an object is equal to the objects mass times its acceleration:

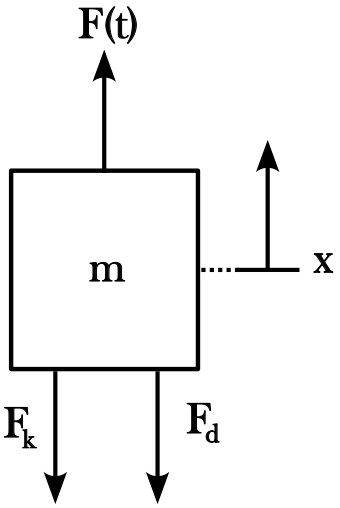

Figure 2.10: The forces acting on the object.

$$\sum F = ma \Longleftrightarrow ma = -F_d - F_k + F(t) \tag{2.12}$$

The displacement is described by x, the velocity (v) is described by the time derivative of the velocity and the acceleration (a) is described by the time derivative of the velocity. The forces acting due to the spring and damper are $F_k = kx$, $F_d = cv$ respectively. With this applied to the system, Eq. 2.12 transforms into:

$$\sum F = ma \Longleftrightarrow m\frac{d^2x(t)}{dt^2} = -c\frac{dx(t)}{dt} - kx(t) + F(t) \tag{2.13}$$

or

$$m\ddot{x}(t) + c\dot{x}(t) + kx(t) = F(t) \tag{2.14}$$

Where

$$F(t) = A_0 sin(\omega t) \tag{2.15}$$

with amplitude A_0 [m] and frequency ω [rad/s]. As stated before, this equation can relate to a mechanism or a material. When related to a mechanism, i.e. a shock absorber, the damping is the rate at which the spring is allowed to compress. When related to a material the damping is the rate at which the material deflects.

As described by Fig. 2.4 the camera is attached to a protrusion on the back-plate. This protrusion allows for rotational movement and vibrations in the yaw- and pitch-directions. In order to attenuate these motions, the camera needs to have damping elements

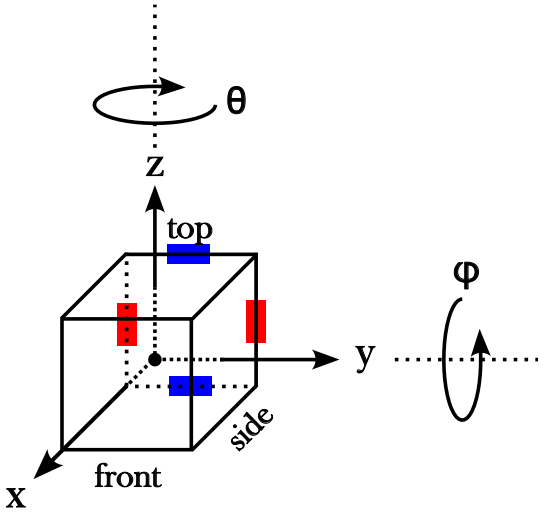

Figure 2.11: The object displayed is in this case the camera.

that reduce them. If the camera is the arbitrary object described in Figure 2.11, then a rotation about the z-axis results in a rotation of the x-y-plane, which can be broken down into displacements of the x- and y-coordinates. The blue and red fasteners represent the placement of damping elements to counteract the rotations about the aforementioned y- and z-axes. This results in a force vector acting in this plane and a combined damping system is required, as described in Figure 2.12.

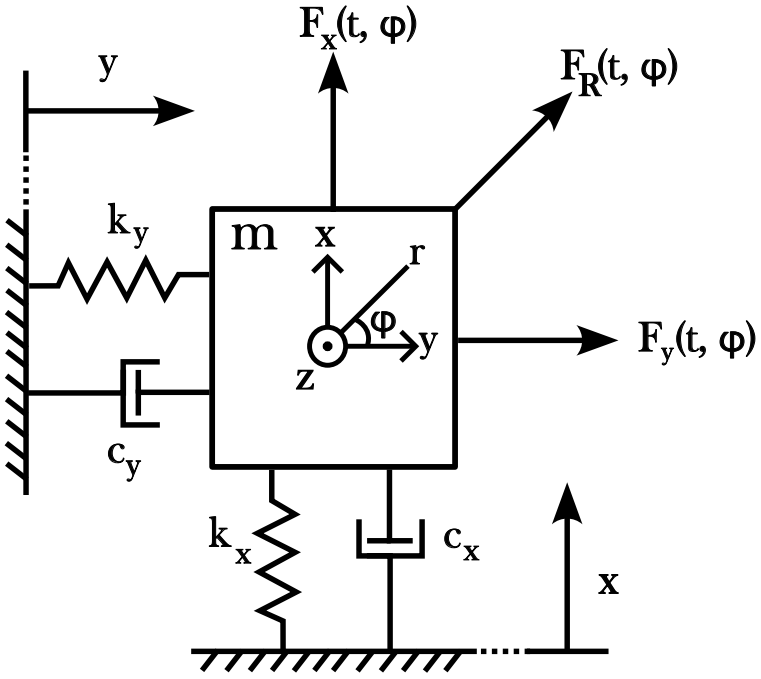

Figure 2.12: A combined damping system to account for multi-axial forces.

The forces acting on the object in Figure 2.12 are of certain frequencies found by analysing the gait cycle. These frequencies are sought to be attenuated through varying the placement and type of damping elements in the configurations seen in Figure 2.11. The types of damping elements differ in stiffness and damping properties.

2.5 Measurement Methods

Gyroscopic Sensors

Gyroscopic sensors[2] are sensors used to detect changes in the angular velocity of a body subject to rotation, and can be used to maintain an orientation of said body. There are several types of gyroscopes such as mechanical, optical and micro-electromechanical gyroscopes. They can be used as standalone component

In consumer products such as phones and cars, the most widely used gyroscope is the MEMS gyroscope. Due to it not utilizing any rotating parts and operating on the principle of vibration and leveraging the Coriolis acceleration, it is easier to minimize the size, making it suitable for applications where the available space is heavily limited. [23]

All gyroscope sensors suffer from accuracy issues to varying degrees [24], such as bias instabilities which is measured in °/s. This instability manifests in a varying measurement at zero reading. This means that when no movement is exerted on the gyroscope, it measures a value that is not equal to zero, as it should be in that case. This is due to integration of noise and other disturbances which are inherent parts of the gyroscopes [25]. This means that there is always an error in angular rate unless the signal is properly filtered.

In the scope of this thesis, gyroscopic measures are used to determine the angular rate that needs to be counteracted. The measured components of the gyroscope are referred to as g_x, g_y and g_z, for the x-, y- and z-axis respectively.

Accelerometers

Accelerometers are used to sense static and dynamic forces of acceleration, with gravity being the most common example of a static acceleration. Compared to static forces of acceleration, the term dynamic refers to changing accelerations, such as the change in acceleration during impact or collision. The change in acceleration is sudden, and having an accelerometer to measure this change can provide useful information regarding the state

[2]Gyro sensors, also known as angular velocity sensors, can detect changes in rotation angle per unit of time. [22]

of the object on which it is attached.

Accelerometers are common in small electronics such as smartphones, where it can be used to determine the orientation and acceleration in directions in order to issue commands. It is also common as a monitoring device for industrial settings [26].

Referring back to Figure 2.6, an accelerometer at rest on a level surface, conforming to the coordinate system displayed, outputs a value of 1g along the z-axis which acts as the force that the surface exerts on the accelerometer. In this case, the output value along the x- and y-axes read 0g since no forces are acting in those directions. In this thesis, the accelerometer values are referred to as α_x, α_y and α_z, and the values are used in testing to evaluate performance of damping solutions.

IMU

Inertial Measurement Units (IMUs) are combined sensors used to measure and determine the orientation and rotation of an object upon which it is attached. There are two types of IMUs, 6DOF and 9DOF, where the 6DOF utilizes a gyroscope and an accelerometer and the 9DOF type has the addition of a magnetometer. The 6DOF and 9DOF, however, do not measure 6/9DOF, but 3DOF rotational movements. To obtain translational movements, more sensors are often needed. The 6 and 9 describes the additively combined axes, i.e. the gyroscope, accelerometer and magnetometer all measure in 3 axes.

The advantage of using a two-sensor solution, i.e. 6DOF IMU, is that there is no need to worry about external magnetic fields interfering with the sensors. The disadvantage is that the measurements tend to be less accurate, considering the magnetometer acts as a complementary component to the gyroscope to accurately measure certain rotational angles [27].

By fusing and calibrating the sensor data, more accurate measurements and information can be obtained compared to using each sensor on its own.

2.6 Electromagnetic machines

When considering active stabilization methods, there is always a need for an actuator able to move the load within a specified, limited space. There are multiple examples, such as linear actuators used for hexapod platform stabilizers [28] and rotational actuators used to stabilize drone cameras [29]. For the purpose of this thesis, focus is on rotational actuators. First and foremost, BLDC-motors are used as a baseline for further development of an angular actuator. The difference here is that while a BLDC-motor can operate at different speeds and unlimited angles, an angular actuator operates within a specified angular span

that is less than 360° in total. This can be achieved by exploring Voice Coil Actuators (VCA) and linear Solenoid Actuators.

BLDC-motors

Brushless DC-motors are motors that, as the name implies, do not have brushes unlike traditional DC-motors but uses a DC supply as traditional motors. Instead, motion is achieved by controlling the magnetic field generated by the coils when current pass through them. Essentially, the rotation is controlled by varying the magnitude and direction of current. The advantages of Brushless DC-motors are that they operate well on high speed and low torque. Coupled with an appropriate position sensor for the application[3] it is a good candidate for precise position control.

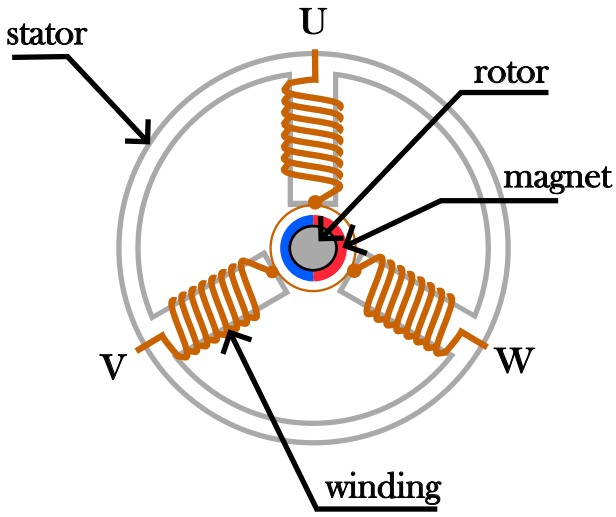

Figure 2.13: A simple BLDC-motor.

Controlling BLDC-motors is done by controlling the magnetic field induced by the current flowing through the windings. In Figure 2.13, there are three phase windings: U, V and W, which means that this specific BLDC-motor is a three-phase motor. In order to control this type of motor, it is necessary to control each of the three phase currents and to be able to measure the rotational position of the rotor. This is done by utilizing a three-phase bridge [30], as shown in Figure 2.14 as well as magnetic sensors, Hall-Effect sensors or sensor-less techniques.

A common control method for a BLDC-motor is Space Vector Modulation, which is a method utilizing Pulse Width Modulated (PWM) voltage signals to vary the direction of current and magnetic field in the stator windings.

[3]As the application of BLDC-motors vary, in this thesis the application is a small-size solution, requiring a small sensor able to accurately read the position of the rotor.

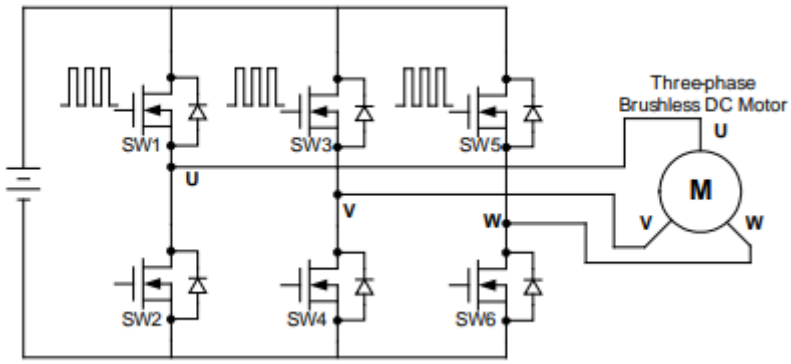

Figure 2.14: A three-phase bridge connected to BLDC-motor [30].

Voice Coil Actuators

Voice Coil Actuators (VCA) are DC-powered linear actuators that work on the principle of the force generated by a magnetic field and a current running perpendicular to this field. The advantages of voice coil actuators are that they do not span a full 360° rotation, but a more limited span of angles. This can be helpful in certain applications such as position control and even angle control. Common uses of voice coil actuators, apart from loudspeakers, include hard drive write heads, due to the limited range of motion that is needed for this application [31]. The structure of a VCA is shown in Figure 2.15, taken from [32].

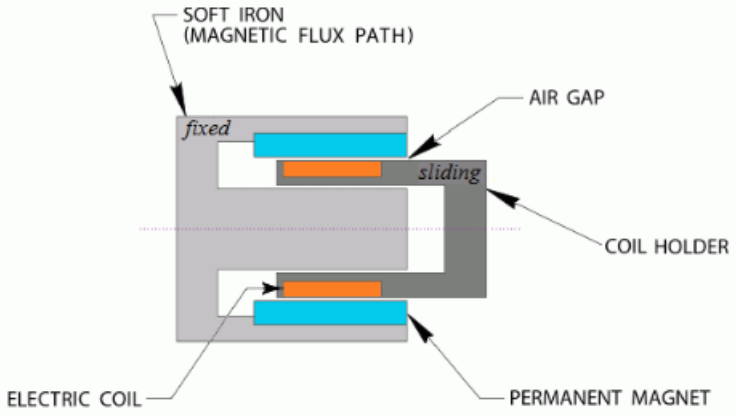

Figure 2.15: The structure of a simple Voice Coil Actuator [32].

VCA:s are simpler to construct and control than BLDC-motors and operate on the principle of the Lorentz Equation (2.16) for controlling the currents' direction and thereby the magnetic field. B is the magnetic field, N is the number of coil turns, i is the current and L is the coil length within the magnetic field. The equation is useful when developing and testing the design of a VCA.

$$F = BNiL \tag{2.16}$$

They are often used in applications that use linear motion but as stated in the previous paragraph, a common application for VCA:s is in hard-disks [33] where the VCA instead is rotary and for a certain span of angles.

Sizing of actuators

When constructing actuators that needs to fit within a confined space, it's important to consider the sizing and how the torque output depends on the sizing. A method for designing actuators is to calculate the torque per unit rotor volume, TRV [34]. Essentially, it produces a ratio between the torque output and dimensions of the rotor, as seen in Eq. 2.17.

$$TRV = \frac{T}{\pi r^2 l} \tag{2.17}$$

2.7 Testing and Data Gathering Methods

In order to create replicable data gathering scenarios, while also keeping in mind the real life applications of the camera, it is deemed necessary to test the generated concepts both when running and walking at a constant pace. To produce the constant pace, a treadmill is used with a setting of 1.8 m/s for walking and 4 m/s for running. These settings produce testing scenarios that are comparable to real life use of the cameras.

Data gathering is done in two parts, firstly by utilizing an IMU and extracting 3-axis gyroscope and 3-axis accelerometer data. This data is then processed using a MATLAB script in order to convert the raw data to meaningful data, that is the gyroscope data in units of deg/s and the accelerometer data in units of m/s^2. The resolution of the gyroscope is ± 250 deg/s and ± 2g for the accelerometer which is important to keep in mind if features of saturation are shown in the resulting graphs. If the data displays saturated behavior, it means that some data is lost.

The second method for data gathering is to record footage while walking and running. This footage is then processed and trace maps are created. The trace maps in turn show an object tracking throughout the footage, and how this object is displaced throughout the footage. The data found here are w- and h-coordinates (y and z according to Figure 2.6 in a two-dimensional w, h- frame, and in the testing context, max(w) = 1920 and max(h) = 1080. As can be concluded from section 2.1, walking and running produce rotational

motion of the camera. When performing image analysis however, the rotational motion is portrayed as translational motion in the mentioned frame, as described in figure 2.16 and 2.17. A rotation ϕ about the y-axis results in a displacement in the h-direction while a rotation θ about the z-axis results in a displacement in the w-direction.

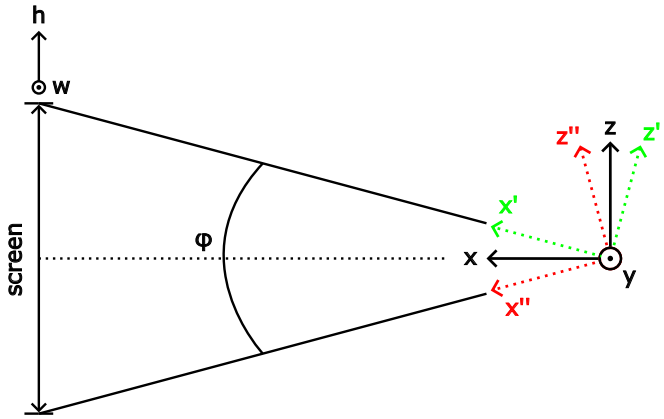

Figure 2.16: The pitch rotation translated into displacement on the h-axis

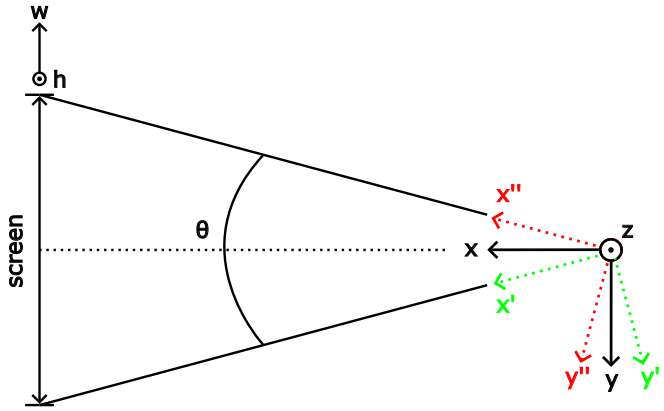

Figure 2.17: The yaw rotation translated into displacement on the w-axis

2.8 Product Development Method

In order to follow a structured approach for generating viable actuator concepts, the product development method described by Ulrich & Eppinger [6] is used. Broadly, their method is described by several phases, as shown in Figure 2.18. As this thesis aims to produce a prototype for the stabilization system, the steps involved in this thesis are up to System-Level Design.

In the Concept development phase, there are several sub-activities, as seen in Figure 2.19. Important to note here is that each step incorporates other aspects such as building and testing models and prototypes in an iterative manner.

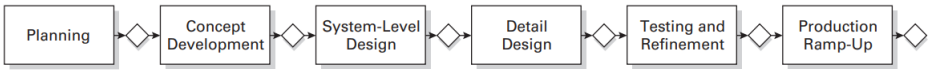

Figure 2.18: The product development process as described by Ulrich & Eppinger [6]

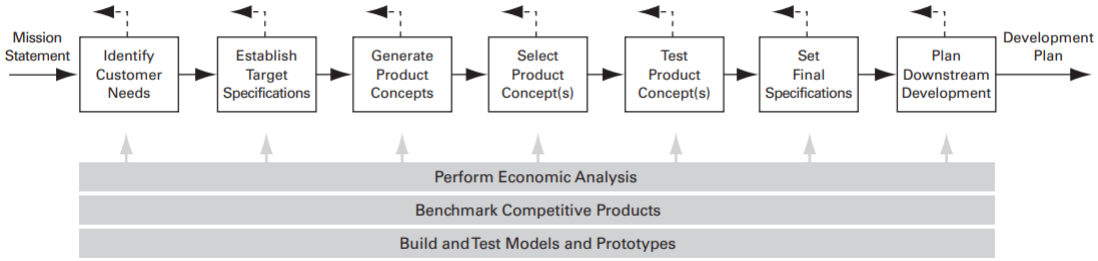

Figure 2.19: The activities in the concept development phase, figure provided by [6].

The first two steps include the activity of specifying customer needs and target specifications. What it means for this thesis is that previous findings combined with a literature review generates a foundation of desired functions, costs, constraints on the product, and accompanying metrics that are to be fulfilled [6]. When this foundation is established, the project moves on to the next step: generating product concepts.

When generating product concepts, a good initial step is to break down the problem in multiple sub-problems. This is called decomposition of the problem [6] and usually starts by identifying the main problem to be solved. The main problem is then broken down into simpler problems, that are easier to handle. In the end, the problem is broken down in a systematic way where solving one problem could lead to solving another, and so on. By breaking down the problem, it makes concept generation easier because it allows targeting of specific sub-systems.

For example, conceptualizing an actuator can be broken down into specifying limits for currents and a required force. This in turn, allows for experimentation with dimensions of the windings, magnets and supporting structures. Finally, specifying the shape and size of the actuator is possible.

When the problem is broken down, a good approach is brain-storming. Here, concepts for either the system at large or sub-systems are generated. These concepts are then evaluated against the project objectives and the aforementioned specifications. This results in multiple viable concepts that can be explored and refined, which is the next step of the concept development process.

Concept refinement is a step which involves further exploration and evaluation of the viable concepts generated during brain-storming, refining the characteristics of the concept

and rejecting concepts that are not suitable to proceed with.

In the System-Level Design phase, defining the product architecture is the main objective. This involves defining the major subsystems that go into the product and selecting and/or prototyping components that are then used within the subsystems. It also involves refining the design of the concept, typically optimizing space efficiency and evaluating component capacities.

Chapter 3

Control System Design

The starting point of constructing the active, controlled mechanical image stabilization system, is data gathering. Here, information about the accelerations and rotational velocities of the cameras' IMU is collected and analyzed. This sets the requirements of the system and by extension, requirements of the components used to construct the system. After researching viable components, testing and constructing and evaluation begins. During prototyping, a control strategy is developed and implemented step by step, making sure to test compatibility between each component and the main control unit. Finally, the control system is incorporated in to the camera with miniaturization as the main focus.

Important to note in this Chapter is that the IMU used to collect data is not the same IMU used to calculate motor angles.

3.1 Data Gathering

Data gathering is done by using a 6-DOF IMU placed within the camera, from which accelerometer and gyroscope readings are extracted. In order to obtain meaningful values from the sensors, a MATLAB-script was written to convert the values from raw data to $^\circ$/s for the gyroscope, and m/s^2 for the accelerometer. Because of reasons discussed in 2.4: Measurement Methods, the gyroscope has slight inaccuracies. Therefore, calibration is performed by placing the IMU in various orientations to measure the deviations from 0. Referring again to Fig. 2.11, the first orientation in which the camera is placed is with the z-axis in the direction according to the figure. The second orientation is with the z-axis rotated 90° clockwise about the y-axis. The final orientation is with the z-axis rotated 90° about the x-axis, from the original position. When a mean deviation had been found, this value is subtracted from the final value. The deviations are presented in Table 3.1

Table 3.1: Gyroscope deviations.

Direction	Deviation [°/s]
g_x	0.49
g_y	-0.23
g_z	-0.01

Although the values obtained at this stage are converted to correct units and tuned with offset, there is still a lot of noise when plotting the data. To counteract this, a moving average filter is implemented. The moving average filter is on the form:

$$\hat{y}(k) = \frac{1}{m}(y(k) + y(k-1) + y(k-2) + ... + y(k-m) \tag{3.1}$$

Where m is the number of data points. Each set of data collected has a size divisible by 2^n, where n = 1, 2, 3,..., yielding m = 2, 4, 8,... which in practice allowed the data to be more strictly filtered in case of an extraordinary amount of signal disturbances or noise. The implementation of this filter, along with all other conversions and calculations are presented in Appendix A. Although this filter gives a clear indication in trends, in certain scenarios it can result in data loss which is necessary to consider when reviewing filtered values. A 180° turn results in a spike in gyroscope data along the axis of rotation, which might be recognized as an outlier instead of an orientation change, meaning the gyroscope in of itself can't be used to keep track of orientation changes.

After calibration, data is gathered through multiple tests and is presented in graphs x-y. The first set of data is collected while running at a pace of 1.8 m/s and the second set of data is collected while running at a pace of 4 m/s. The data relevant to the active control system is gyroscope values measured around each axes, as described in Fig. 3.1 and 3.2.

As can be seen when comparing Fig. 3.1 and Fig. 3.2, the difference in amplitude is approximately 50°/s about the z-axis, indicating a rather high increase in rotational movement between the two cases. In general, an increase is expected by increasing speed due to natural biomechanics. Running induces more motion on the body than walking and thus, running is the worst case scenario for stabilization.

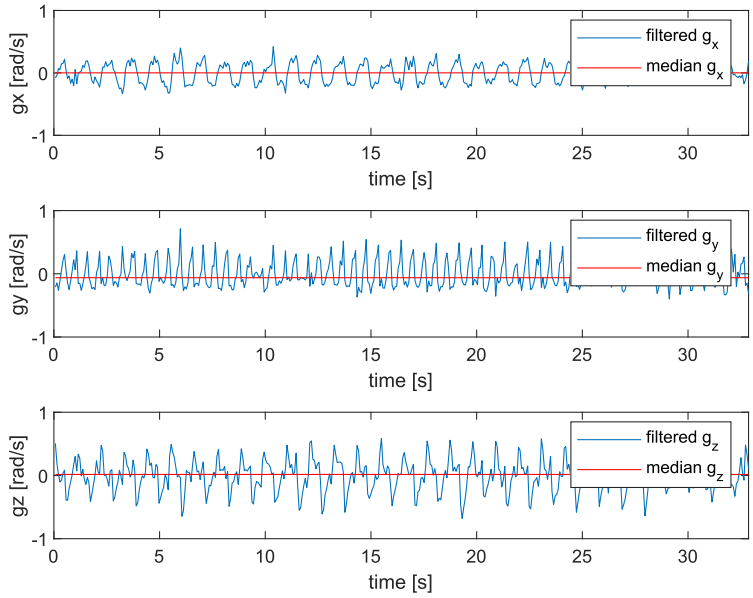

Figure 3.1: Angular velocity about each axis, walking at 1.8 m/s.

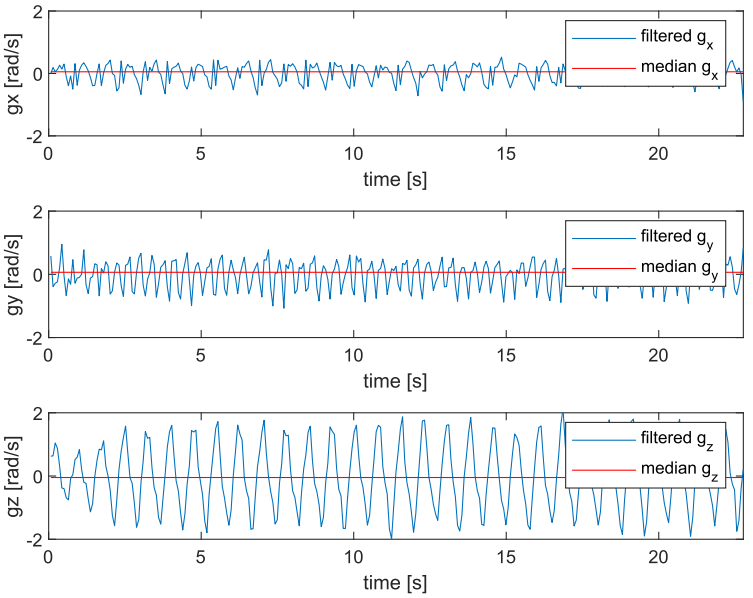

Figure 3.2: Angular velocity about each axis, running at 4 m/s.

3.2 Single-axis Image Stabilization Specification

The active system only controls the ISLA and needs to compensate for rotational velocities up to 120 °/s, while also compensating an angular range of ±25°. A necessity for the system is to be able to account for a change in orientation. In this scope, a change in direction is defined as 90° orientation around the z-axis defined in section 2.2.

The active system should be non-obstructive, meaning any new mechanical parts used should affect the current shape of the camera as little as possible. The choice of using a BLDC-motor (Table 3.2) is because it has been proven to be effective [4]. Although this is the same motor that has been used in earlier work, experimentation with the aim of reducing the current consumption and required voltage is performed. Using the same BLDC-motor is a choice made to reallocate time from constructing an actuator to experimentation and also offers continuity in the sense that there has been experimentation performed on the actuator previously. It also allows for constructing a functioning active MIS system and to further test its' capabilities within the given time frame. All other components are chosen with size reduction in mind.

The general structure that constitutes the control system is firstly a micro-controller (Table 3.2). The micro-controller is responsible for communication between components and running the control algorithm for the motor. Because of the motor type and for the purpose of position control, a motor driver is needed. The motor driver (Table 3.2) takes 6 PWM-signals from the micro-controller, amplifies these signals to match the voltage required by the motor and outputs 3 phase voltages directly to the motor. The necessity of the driver is due to the limited current output from the micro-controller, as there is a limit on how much current each pin can output. With the selected motor driver it is possible to output as much as 2A if needed, where as the maximum allowed current for one motor is 1A [35], meaning the driver can output well above the limit. The motor driver also acts as a shield [36] between the micro-controller and motor, by drawing the required power from an external battery-source and having internal diodes to ensure that current flows in the correct direction. To achieve feedback control of the system, a sensor that can measure the rotational velocity and angle of the motor is needed. To obtain a desired angle, an IMU is used to measure the angle of the body and this angle is then used as an input to the motor control. In this case, the IMU is considered fixed to the body of the wearer and the motor is free to rotate. Specifically, according to the control strategy, it is free to rotate the opposite angle that the IMU measures, as seen in Fig. 3.3. The components described to be used in the active mechanical stabilization system are listed in Table 3.2. In Fig. 3.7, a block diagram showing the connections between each component is shown.

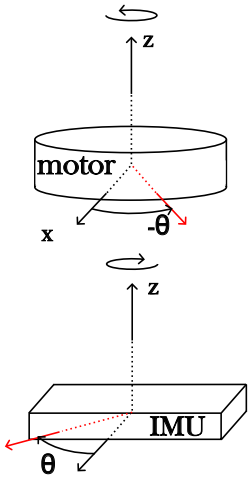

Figure 3.3: The operating principle for the control system: the IMU detects movement to the right, the motor must turn left.

Table 3.2: Description of components used in the construction of a prototype.

Component	**Purpose**
EM3215 BLDC-motor [35]	Actuator to control ISLA forward position.
Raspberry Pi Pico [37]	Main control unit responsible for all functions.
TMC6300 3-Phase Motor Driver [36]	Routing control to the actuator.
AS5048B Magnetic Sensor [38]	Tracking rotational angle of the actuator.
ICM-20948 9-dof IMU [39]	Tracking rotational angle of the body.

3.3 System Communication

The system communication between the micro-controller and the peripheral devices needs to be reliable in order to measure angles from the IMU, the rotational angle given by the magnetic sensor as well as to issue orders to the motor driver. In this thesis, the controller is referred to as the *main unit* and a peripheral device is referred to as a *sub-unit*. There are multiple ways for sub-units to communicate with the main unit, among them SPI or I^2C.

SPI (Serial Peripheral Interface) works by setting up communication between the main unit and a sub-unit using four wires. Here, the data is synchronized on the falling or rising clock edge provided by the main unit and it allows for bi-directional data transfer [40]. Each wire provides one signal and the four signals are:

- Clock (SCLK)
- Chip Select (CS)

- Main in, sub out (MISO)
- Main out, sub in (MOSI)

While most main units allow for connecting several sub-units, the issue with SPI is that each added sub-unit requires a different Chip Select input and output, meaning that a configuration of one main unit and two sub-units result in using eight wires, as shown in figure 3.4. The problem with adding more sub-units is then obvious, as most micro-controllers simply do not have enough CS-wires to support more than 1-2 interfacing devices.

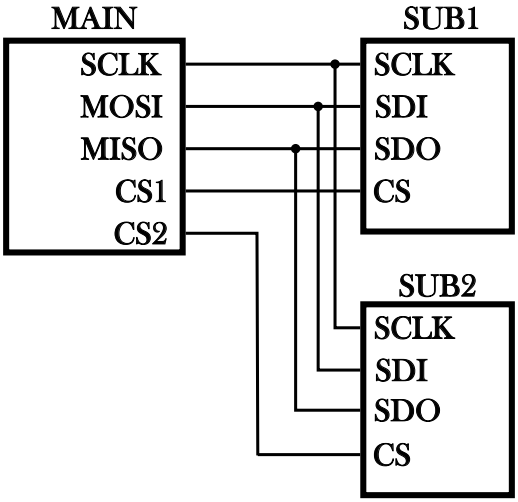

Figure 3.4: SPI structure to showcase the problem with multiple peripheral devices.

The alternative, I^2C, utilizes only two inputs, excluding power and ground, regardless of how many peripheral communication devices are connected. Instead the devices need to have different addresses which are at times set and can be found in accompanying datasheets, and can be configured through optional pins on the devices.

The largest advantage that SPI has over I^2C is the clock frequency and while it's chip dependent, SPI has higher clock frequency than I^2C. Depending on the application it might be necessary use SPI over I^2C. However, if for example the I^2C clock frequency is 400kHz, it means that the value a sensor transmits is updated every 2.5 µs, which is often enough to achieve stable communication between position sensors, IMU and the micro-controller.

Actuator

The chosen actuator is a BLDC-motor in an outrunner[1] configuration. An inrunner configuration would be preferred if the actuator is small enough to fit inside the camera housing

[1] An outrunner motor has the rotor on the outside of the stator, as opposed to traditionally being inside the stator with an output axle.

as it would enable the ISLA holder to be smaller. However, the dimensions of the actuator used exceeds the available space, and whether it is an outrunner or inrunner does not matter. Essentially, what is important when wanting to control a motor of this type is to accurately control the 3 phase currents. The actuator is an EM3215 BLDC-motor and its' characteristics are presented in Table 3.3. The reason that only the start torque is shown is due to it being the only specified torque in the datasheet, thus providing a basis for torque calculations.

Table 3.3: Electrical characteristics of the motor.

Poles [-]	Rated Voltage [Vdc]	Start Torque [Nmm]	Start Current [mA]
8	7.4	31	800

There are several drawbacks with the selected actuator. The main drawback is that while the size is small, it would be desirable to find an even smaller actuator that could be integrated into the camera housing. This could be possible to achieve by designing an actuator that doesn't have a full angular span, i.e. 360°, and instead have a set span that covers the range of angles specified in section 3.1. This is further investigated in Chapter 5, by aid of simulation and calculations. However, in order to create a prototype that demonstrates the capabilities of the new system, this motor is used to achieve active image stabilization. Another drawback of the chosen actuator is the current draw. The actuator needs 110 mA at 7.4 V to function for angular differences, according to the datasheet [35]. As the motor is not current controlled, at start-up it has a start-up current of 800 mA. Through experimentation with both voltage and software, this start-up current spike is sought to be eliminated as the start-up position can be found by use of a magnetic sensor and then manually declared in code. The motor torque constant can be calculated as follows, using the start-up values found in the datasheet [35]:

$$K_T = \frac{T_{start}}{I_{start}} = \frac{31Nmm}{800mA} = 0.03875 \tag{3.2}$$

This constant can then be used to calculate the expected torque when varying voltage and current. Similarly, when starting the motor at nominal voltage using the h-bridge described in Fig 2.14, where SW1 and SW4 are closed and the measured resistance between the U and V-phase is 9.25 Ω, the required current input is:

$$\frac{U}{R} = I \Longrightarrow \frac{7.4V}{9.25\Omega} = 0.8A \tag{3.3}$$

Which means that lowering the voltage applied consequently lowers the required current.

Since this actuator utilizes three currents to rotate, it needs a driver card that can

output 3 separate signals while also drawing its' input current from a source other than the micro-controller. The chosen motor driver card takes 6 PWM-signals as input and outputs 3 phase voltages, while being able to do so at an operating voltage of 7.4 Vdc. A large part in constructing the active system involves experimenting to test the operating current and operating voltage, and to investigate how the system behaves when varying the voltage and current. The goal of this is to determine if it is possible to drive the motor and employ control algorithms at lower voltages, while also achieving a low current draw. The purpose is to be able to run the system with one peripheral voltage sources (a battery) and use a micro-controller as the sole voltage and current source for sensors, which is capable of supplying 3.3 Vdc and a maximum of 40 mA per output pin [37]. This is further explained in Section 3.4.

Micro-controller

The choice of micro-controller is based on a few requirements:

- Needs to be able to control the position of the given actuator.
- Needs to be small, on the cm scale.
- Should have the capability of controlling multiple[2] actuators at once.
- Needs to have a sufficiently large flash memory such that all functionalities can be implemented and stored on the device.

The chosen actuator is driven by 3 PWM-signals. This means that in order to run a single actuator, the micro-controller either needs to be configured to control the actuator directly or indirectly, through the use of a driver card. As stated in section 3.2, a driver card that takes 6 signals as input and outputs 3 signals, the micro-controller needs to be able to output at least 6 PWM-signals.

When it is desirable to minimize the size of the micro-controller, there are multiple candidates but many are excluded when also considering flash-memory size. For example, an Arduino Nano might seem like a good candidate at first. It is a compact micro-controller with 6 PWM-outputs and both 5V and 3.3V logic outputs, and a flash-memory size of 32 kB. As the micro-controller is responsible for communication with multiple peripheral devices, it needs to be able to compute and process real-time data input from sensors. The proposed active system requires two sensors, one to control the motor and one to calculate the angular deviations when moving. With all of this in mind, it's better to go for a larger

[2]Some micro-controllers have up to 16 PWM-outputs and with the appropriate driver(s), multiple actuators of unspecified type can be controlled.

flash memory size in order to ensure that all required sub-routines can run without running out of storage. A Raspberry pi Pico (RP2040) has a flash-memory size of 2 MB and it is possible to configure the GPIOs of a Raspberry Pi Pico to output a maximum of 16 PWM-signals at once. This means that if configured correctly, a Raspberry Pi Pico is capable of running multiple motors granted there is an external power-supply.

IMU

The IMU needs to be able to convert the read data into quaternions in order to accurately estimate the angle, within $\pm 1°$. Quaternions is, as mentioned in Chapter 2.2, is a way of keeping track of orientation in three-dimensional space. As the proposed system only utilizes one motor to control the yaw angle, ψ about the z-axis, the calculations become rather simple as q_x, q_y and q_z are calculated via the IMUs DMP unit and extracted by utilizing built-in functions. From this, q_r can be calculated as follows.

$$q_r = \sqrt{1 - q_x^2 - q_y^2 - q_z^2} \tag{3.4}$$

Now, the sequences for the control system is only rotations about the z-axis, meaning that the yaw angle can be calculated as seen in equation 2.11:

$$\psi = 2 * tan^{-1}(\frac{q_z}{q_r}) \tag{3.5}$$

For analysis purposes, it would be interesting to extract the angles calculated. However, due to limitations in storage capacity of the selected micro-controller this is not possible as it has no built-in storage capacity. It would be possible to add a circuit for an SD card holder, but that is not included in this thesis.

Sensor

The magnetic position sensor for measuring the actuators rotation uses the I^2C protocol to communicate efficiently, while also enabling the circuit connections to be simple and non-obstructive to other parts of the system. It is a key part in obtaining feedback control, by supplying the control loop with the current angle of the actuator. The chosen magnetic sensor is the AS5048B Magnetic Sensor which is a 14-bit rotary sensor, and as such it has 16384 positions/rev giving a resolution of 0.022° [38]. It functions by attaching a 2-pole magnet to the rotor of the BLDC-motor and placing the sensor beneath the magnet at a vertical distance of, in this thesis, 0.5 mm.

Component Overview

To provide an overview of the components chosen, Table 3.4 is constructed. Here, key electrical characteristics are presented. The voltages and current consumption of the components have been found through experimentation. However, for the IMU and Magnetic Sensor, the voltage and current are stated as specified in their respective datasheets. The power consumption is calculated to be a total of 0.472 W.

Table 3.4: Electrical characteristics of the selected components.

	EM3215	**RPi Pico**	**TMC6300**	**AS5048B**	**ICM-20948**
Voltage [V]	3.7	3.7	3.7	3.3	3.3
Current [mA]	6-26	40-42	6-26	15	3
Power [W]	0.096	0.22	0.096	0.05	0.01

3.4 Control Methods

PID

PID is an automatic control method that is commonly used in actuator and motor applications and used for both velocity and position control in this context. It has a simple structure, but requires sensors to measure the error of the value that needs to be controlled, whether it is a velocity of a motor, the extension of a linear actuator or the level of a fluid. In this thesis, the PID control is implemented to control the position of the actuator, where it uses the data from the IMU to calculate the desired angle and the data from the magnetic sensor to calculate the actual angle. A PI-controller is implemented for the velocity control. As such, the magnetic sensor acts as a feedback sensor for both controllers.

A PID-controller takes an input signal, often referred to as a reference signal, which is the desired value of the output signal. This input signal is taken into the system, where there is a model of the actuator and the PID-controller and outputs the compensated signal. Fig. 3.5 describes the structure of this control.

With $y(t)$ as the output signal, $r(t)$ as the reference signal, the error in the control is $e(t) = r(t) - y(t)$, with $e(t)$ having a desired value of 0, the error is what is fed into the PID controller block. With u(t) being the output signal from the PID block, it is on the form:

$$u(t) = K_P * e(t) + K_I \int_0^t e(\tau)d\tau + K_D \frac{d}{dt} e(t) \tag{3.6}$$

Or equivalently, for tuning algorithm purposes:

$$\begin{cases} u(t) = K_a(e(t) + \frac{1}{T_I}\int_0^t e(\tau)d\tau + T_D\frac{d}{dt}e(t)) \\ K_a\frac{1}{T_I} = K_I \\ K_aT_D = K_D \end{cases} \tag{3.7}$$

The method used for tuning the PID-controller is the Ziegler-Nichols method [41], which builds upon starting with proportional gain and choosing K, such that the system self-oscillates. As can be seen in Equation 3.5, the same K_a is then used for the K_I and K_D terms, with T_I and T_D chosen as seen in Table 3.4. In the table, K_0 is the initial K_P value used to induce self-oscillation in the system.

Regulator	K_a	T_I	T_D
PID	$0.6K_0$	$\frac{T_0}{2}$	$\frac{T_0}{8}$

Table 3.5: Ziegler-Nichols tuning parameters according to Glad & Ljung [41]

While this method worked for tuning the velocity control of the motor, it was further complicated when introducing a PID-controller to control the angular position. This type of control is called cascade control, and cascade control is a method for controlling multiple parameters, resulting in utilizing as many PID-controllers as control parameters. Due to having to calibrate the velocity control at the same time to achieve smooth control, the tuning of the cascaded controllers were done experimentally until satisfaction. The control structure is described in Fig. 3.5, where a certain voltage is set for a corresponding speed. Since the motor drive operates without load and speed, the system's power consumption is so low that there is practically no need for current and subsequent torque control. In this regard, this report does not present practical experience in implementing current control, as it has not been used. Hence, the current control part of the structure is omitted.

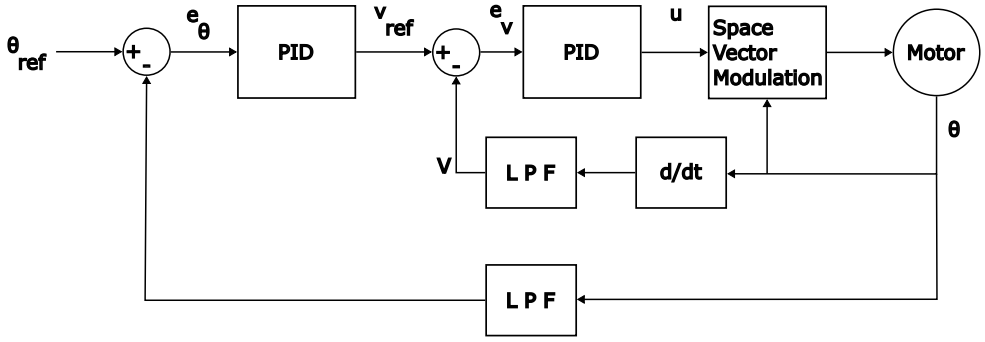

Figure 3.5: The cascade structure of the controller.

Space Vector Modulation

The control of BLDC motors isn't trivial, but often there are several ways to control the three phase motor. One of those ways is Space Vector Modulation (SVM), which is used in this thesis. The driver used is controlled by the micro-controller, which performs the calculations shown in Eq. 3.6 and 3.7, and is given PWM voltage signals.

The premise upon which SVM works is to control the torque. Torque control, which is essentially current control, is well explained in Power Electronics - Devices, Converters, Control and Applications by Alaküla et. al [42]. As stated previously however, this is handled by a software library and omitted in this thesis. Essentially, SVM is done by transforming the three phase currents i_U, i_V and i_W into two currents controlling each parameter respectively. However, the outputs of the micro-controller are PWM-signals that emulate AC voltages for each of the three phases, similarly to Fig. 2.14 where each gate-pair represents U, V and W-voltages. The result is a voltage vector which is dependent on each of the gates on and off time (as a percentage). Each phase voltage can be seen as vector and the vector sum of these vectors is the voltage vector that controls the motion. The current transformation is done by using the $\alpha\beta$-transformation followed by a dq-transformation [43]:

$$\begin{cases} i_\alpha = \frac{3}{2} i_U \\ i_\beta = \frac{\sqrt{3}}{2} i_V - \frac{\sqrt{3}}{2} i_W \end{cases} \tag{3.8}$$

$$\begin{cases} i_q = -i_\alpha sin(\theta) + i_\beta cos(\theta) \\ i_d = i_\alpha cos(\theta) + i_\beta sin(\theta) \end{cases} \tag{3.9}$$

Where i_q and i_d are the torque controlling and flux controlling currents, respectively. The angle θ is the angle of the rotor at a time instant. The purpose of these transformations is to simplify calculations by converting alternating currents into DC like controllable currents. Although the motor used is a BLDC-motor, the characteristics for which it works is similar to that of a Permananent Magnet Synchronous Machine (PMSM), because of the three-phase currents that drives the BLDC.

The currents are calculated and then the inverse of the previous transforms are performed. The control block then outputs the three desired AC like PWM voltages u_U, u_V and u_W. The idea of SVM is to alternate the time each voltage output is active, corresponding to a percentage between 0 and 100% [44].

3.5 Testing of Components

Implementing the functions required to control the angle of an actuator is broken down into smaller sub-functions. Initially, each component is tested on its own, by connecting it to the μ-controller and writing simple programs that test the main functions required in the proposed system. As stated in previous sections, it is important that the communication worked efficiently when using the I^2C-protocol. This is tested by connecting the components whose data needed to be read and having the data stream open to the console in real-time. Being able to read the data in real-time is not a necessity when implementing the actual control, but it is crucial for debugging reasons and understanding the type of data being received. This aids in converting the data to meaningful values that can be used in calculations.

When testing the actuator, there are several stages that need to be tested. As an initial test, the parameters regarding the actuator such as operating current and voltage is set according to the datasheet provided by the manufacturer. After concluding that the actuator did indeed work according to the values provided, varying of the voltage was performed. In order to not damage the micro-controller, a separate power source is used throughout the testing. First, a DC Power Supply is used, where the output voltage was set to 7.4V, as specified in the datasheet [35], and the current output was limited to 1A. Here, the voltage was brought below the operating voltage specified in the datasheet, and ultimately it was concluded that the motor can run on a minimum of 3V without any obvious issues appearing, such as stuttering motion which was observed at voltages below that. The current output at this level was at start-up 500 mA and operating current in the range of 10-30 mA. The spike in current at start-up was due to a sub-routine which ran for 5 seconds and calibrated the electrical angle in relation to the mechanical angle each time the system was powered on. However, after implementing another sub-routine which sets the electrical angle instantly the current draw could be reduced to be within the operating range, with a short initial spike at start-up which is calculated to be 400 mA according to Eq. 3.3 and substituting 7.4V with 3.7V. This spike only appeared if the rotor was not in the forward facing direction when connecting the battery. The electrical angle was calculated by utilizing a program created by the authors of SimpleFOC [45] and is explained by the flowchart described in Fig. 3.6. Important to note about the figure, is that if the result is a FAIL the flowchart proceeds to the block "Align Done" without setting the correct electrical angle.

In conclusion, it is possible to power both the μ-controller and motor driver card with the same supply voltage, a 3.7 V battery. Being able to power the entire system with a single power source means that it is possible to scale down the system to its largest component, namely the battery. To exemplify the capabilities of the BLDC-motor, the

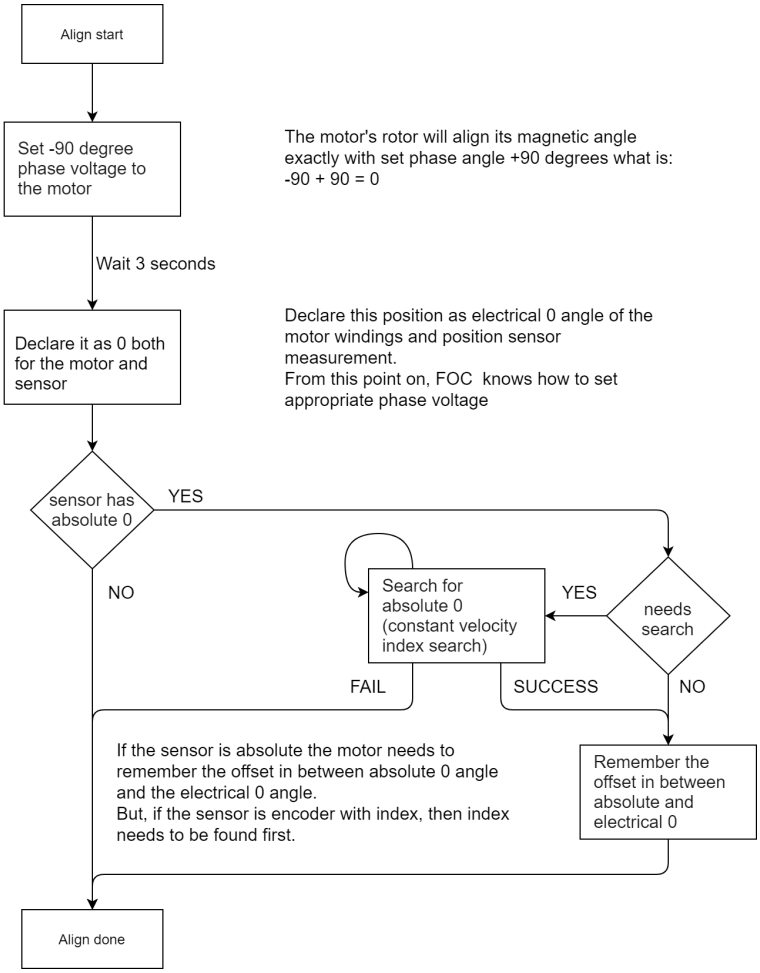

Figure 3.6: The method for calculating the electrical angle of the motor. Graph taken from SimpleFOC docs [45].

start-up torque (which is the only specified torque and hence the only basis for calculation) is now calculated as follows, with 3.7 V instead of 7.4 V as the voltage and with the motor torque constant calculated in Eq. 3.2:

$$T_{start} = \frac{3.7}{9.25} * 0.03875 * 10^3 = 15.93 Nmm \tag{3.10}$$

Which at start up uses 0.4 A for a brief moment to position the ISLA forwards, if it is not already facing forward. Another value of interest for further development of an actuator is the TRV, as described by Eq. (2.17). The TRV can be calculated for the use case of this thesis as follows:

$$TRV_{3.7V} = \frac{T}{\pi r^2 l} = \frac{15.93}{\pi 16^2 9} = 0.0022 \frac{Nmm}{mm^3} = 2200 \frac{Nm}{m^3} \tag{3.11}$$

When each component has been confirmed to fulfill its function on its own, all components were incorporated according to the circuit diagram in Fig. 3.7. Testing of the full circuit

was performed and smaller programs were written to make sure that each component worked as expected when simply submitting a desired velocity of 2, 4, 8 rad/s to the motor driver card. At this point, the initial rotor angle was of no concern and the implementation of position control is described in the Section 3.6.

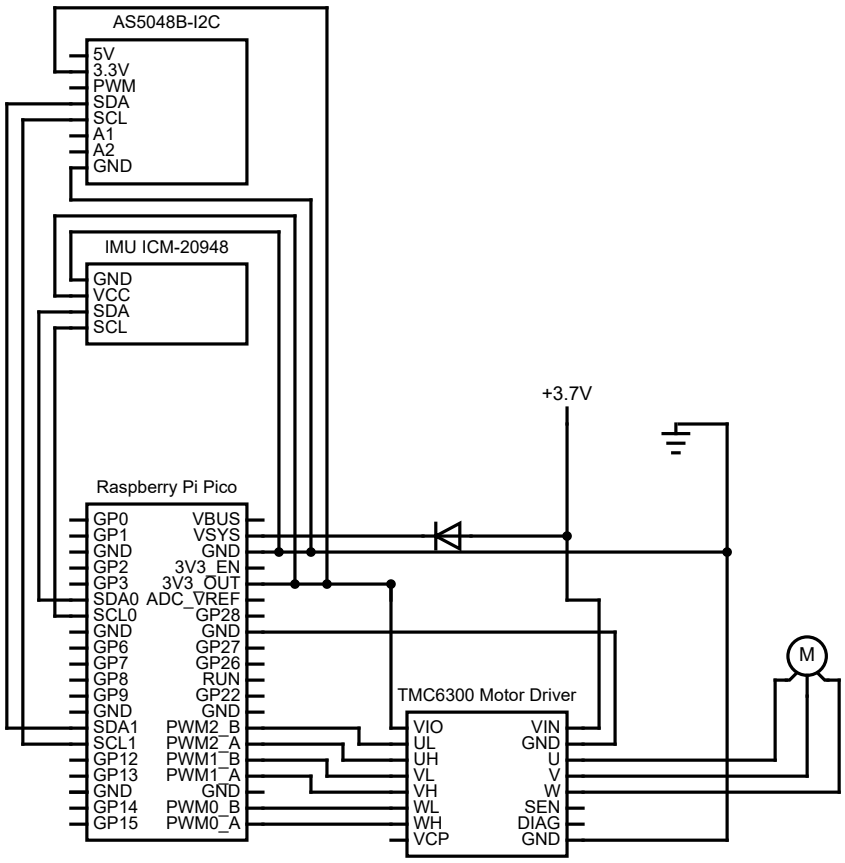

Figure 3.7: The complete circuit structure.

3.6 Software Implementation of Position Control

The position control algorithm for the micro-controller is written entirely in C++, allowing the utilization of component-specific libraries for the μ-controller and the IMU. For the FOC control algorithm, there is a library designated to use with BLDC-motors. The strategy for controlling the motor angle is to simply counteract the angle transmitted by the IMU. This meant that if the IMU transmits an angle θ, the motor should compensate it by rotating with the negative angle, $-\theta$. The reasoning behind this is that it is a relatively simple control method which allows for fine-tuning the control parameters without having to take the algorithm for angle calculation into account. However, the control method used to

structure the PID control is a cascade structure, meaning the schematics are a bit different from a regular PID-controller scheme, as it includes multiple PID controllers in series as described in Fig. 3.5, instead of a single PID-controller.

The objectives of the controller and actuator are:

- Measure the deviation in angle from the forward direction, i.e. along the x-axis.
- Use this angle as input to the PID controller.
- The actuator compensates the angular deviation by rotating in the opposite direction.
- Have the capability to update the forward direction, meaning recalculating the cameras' coordinate system to match the coordinate system of the body in the event of a $\pm 90°$ rotation.

The system needs to keep track of orientation and which direction is considered the IMU's forward which is its' x-axis. If it does not, the starting position will always be considered forward, as for instance making a right turn around a corner, the lens is still pointing towards the forward direction before the right turn. In order to make a difference between orientations, a Finite State Machine (FSM) is implemented. This FSM works on the simple premise that a rotation larger than $90°$ results in switching to one state, and a negative rotation of the same magnitude results in switching to a different state. In each state, the control signal has the orientation change, that is $90°$, subtracted or added depending on the direction of change. After handling the change, the system returns to its' original state where the angle is controlled as described earlier. The FSM is described in Fig. 3.8.

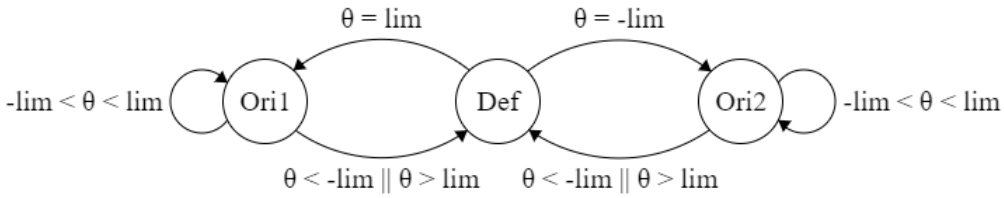

Figure 3.8: The FSM used to track the forward position.

In the software implementation, the desired motor angle is calculated according to Equation 3.3. It is then passed to the control loop.

3.7 CAD of Supporting Structure

For the control system it is deemed important to not obscure any camera functions, such as displays and buttons. It is decided that the system is to be mounted on the front of the camera, utilizing the shape of the camera and mounting solutions to minimize the size. Fig. 3.9 shows the final prototype of the mounting solution. All coloured items in the figure are electronic components. Not shown in Fig. 3.9 are the camera and camera module.

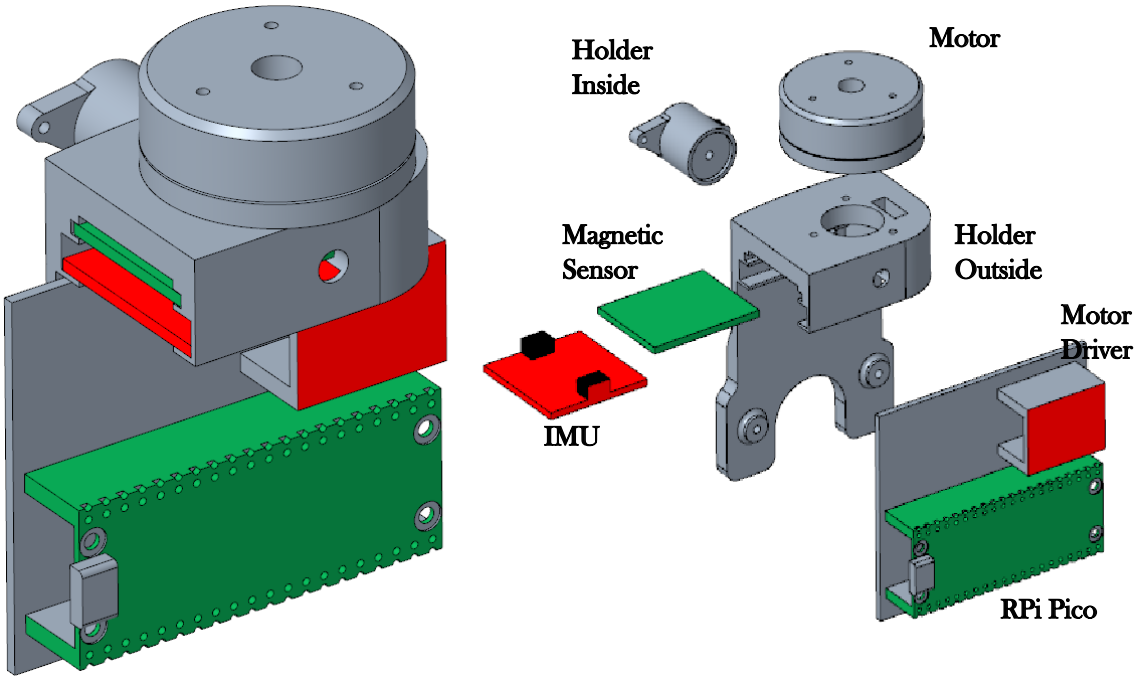

Figure 3.9: The combined mounting solution for holding the active MIS system, with an exploded view showing each component.

3.8 Results of Active Image Stabilization

The implemented system is able to be driven by a 3.7V battery with a maximum current output capacity of 2A. To power the RPi Pico and its' auxiliary components, a constant current of 54 mA were drawn from the battery. When measuring the current draw of the system, it varies between 60 mA to 80 mA, dependent on if the camera is moving or in stand-still. This also means that the start-up current has been eliminated by setting the electrical angle according to position sensor data. By subtracting the control systems current draw, the motor driver used 6-26 mA to control the motor angle. This indicates that under no-load conditions, such as in this use case, the specified motor can be driven on half the voltage specified with a current draw that is lower. This is due to the lower

amount of power needed to drive the motor. In Fig. 3.10, the prototype is shown mounted onto the camera.

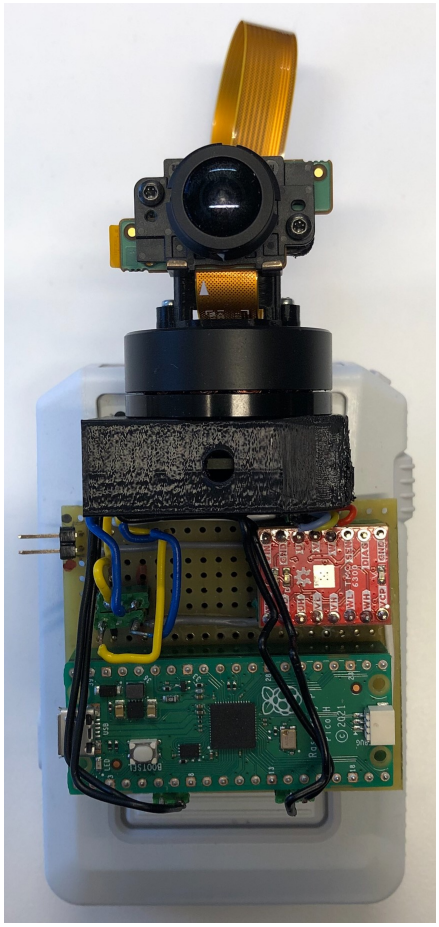

Figure 3.10: The prototype mounted to the camera.

Analysis of the video feed is performed to assess the performance of the actuated system. The video feed has the resolution 1920 x 1080 (width x height) and the method for measuring performance is to track an object in the video feed, trace out its' path and extract the data points into a .csv file. This file included one column for the values of x and one column for the values of y, where x and y is the displacement in width and height, respectively. All graphs are according to the same scale, where the center is in the middle of the graph. This corresponds to the test case, where the tracked object was placed in the middle of the video feed as can be seen in figure 3.11. Each video was recorded for approximately 40 seconds to safely be able to cut the length without losing any valuable data. Each video was cut to be 20 seconds long, in order to extract the same amount of data points for each trial.

Note that the graphs (Fig. 3.12-3.15) are magnified by a factor of 6, to increase visibility and comparability. In Fig. 3.12 and 3.13, the trace maps of the image analysis for the case

Figure 3.11: The object being tracked in analysis.

of no control are presented. The red line shows one highlighted period. The cause of the uneven effect is due to inherent biomechanics, as described in chapter 2.1. In Fig. 3.14 and 3.15, the trace maps of the image analysis for the cases with MIS and BLDCM position control are presented.

Table 3.6: Comparison table of the different cases presented.

	$\|max(x) - min(x)\|$ [px]	$\|max(y) - min(y)\|$ [px]
Running without control	501.2	129.0
Walking without control	199.2	62.0
Running with control	153.1	134.7
Walking with control	82.3	43.0

Figure 3.12: Running without control.

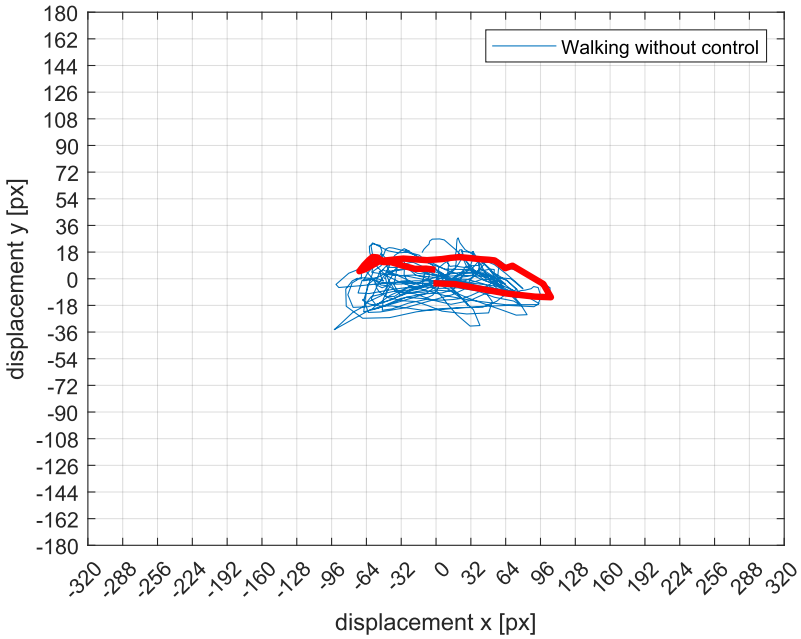

Figure 3.13: Walking without control.

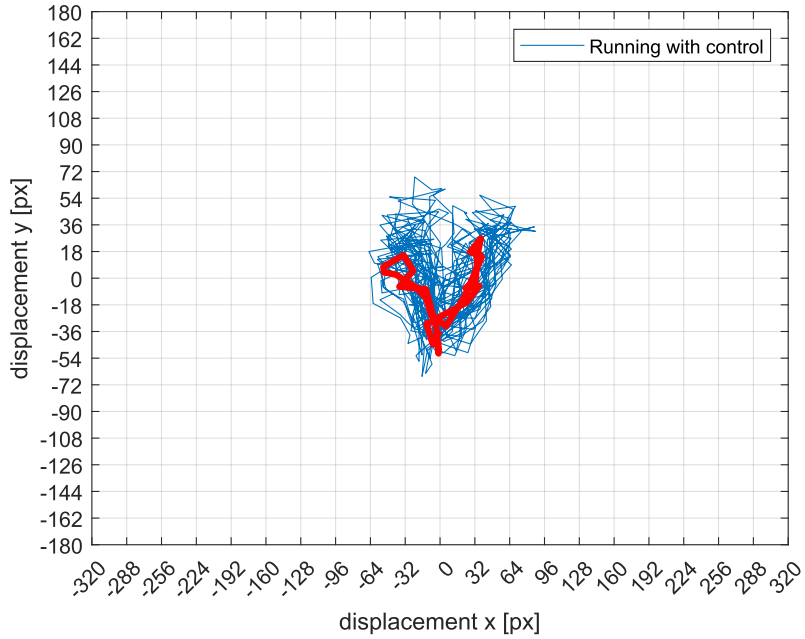

Figure 3.14: Trace map for the test case when running with control.

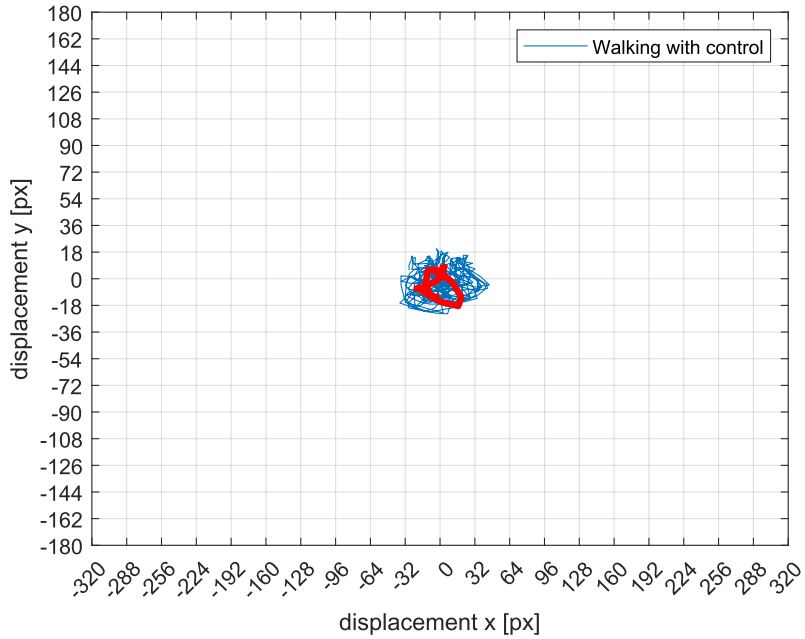

Figure 3.15: Trace map for the test case when walking with control.

As can be seen in the Fig. 3.14, Fig. 3.15 and in Table 3.6, there is significant reduction in the movement of the ISLA when control is applied.

For Fig. 3.14, the spread in the x-coordinate is reduced while the spread in the y-coordinate is somewhat larger. This is likely a result of variation in gait pattern. Although the test scenarios were designed to eliminate as much of the variation as possible, there are some parameters that keep varying simply due to variations in the gait pattern.

Chapter 4

Passive Damping System Exploration

To account for vibrations and rotational deviations in other directions than the one controlled by the active system, a passive damping system is sought to be implemented. The approach is to test multiple different conceptual damping systems and analyze IMU data, by utilizing a script written in MATLAB to extract the gyroscope and accelerometer data from the IMU. The purpose of this is to be able to visualize the disturbances exerted on the camera by walking and running.

As the method employed is exploratory, all values recorded from the gyroscope are of interest at first to identify what impact the damping solutions have.

The damping solutions include using soft materials, springs and combination of these two types. The soft materials include to foam and silicone (Shore 40A). The silicone is significantly stiffer than the foam. A comprehensive list and ranking is presented as well as a prototype.

Through the processing of video and each frame, it is possible to track an object throughout the duration of a recording. This enabled the data processing of the tracked path, essentially allowing to gather the tracked path as data points for comparative purposes. Important to note is that the data points are projections and have 2 dof, i.e. each point is composed of two coordinates, x and y. The coordinates were converted into arrays which were then used to plot the ISLA movement using MATLAB.

4.1 Concepts for damping

Although this chapter is focused on exploration, some basic ideas need to be set for the damping concepts. Firstly, the placement of the damping concepts is such that it supports the back of the camera. This means fastening it to the current mounting solution, which has the current camera attachment solution attached to a back plate, see Fig. 2.4. No damping configuration is directly attached to the ISLA. However, due to how the damping configuration is applied, it is always under light to moderate compression when in contact with the camera, similar to a how a pre-compressed spring limits the stroke length.

Each damping solution and their respective material is presented in Tab. 4.1. The placement (Fig. 2.11) refers to where around the protrusion the material is placed. The more precise dimensions for the silicone configuration is because of using a mold that was designed for casting, while the foam solutions were cut as pieces from a larger sheet and rolled into cylindrical shapes.

Table 4.1: Configurations of damping materials.

Material	**Dimensions (w, h, d) (mm)**	**Placement**	**Configuration**
PE Foam	(40, 10, 10)	Bottom	1
PE Foam	(40, 10, 10)	Sides	2
PE Foam	(40, 10, 10)	Bottom and sides	3
Silicone	(32.5, 12.3, 11)	Bottom	4

4.2 Data gathering and Analysis

The aim of the data gathering is to construct comprehensive sets of data for analysis and comparison. The materials used to test the damping were springs, elastic foams of different types and the combinations of these different materials. The results are presented and compared to the base results shown in Fig. 3.12 and 3.13, the tracing of the ISLA movement is presented without any form of damping. Note that the tracing graphs are magnified by a factor of 3 for better visibility in order to provide clear trajectories for analysis.

The trajectory of the projection of the movement relative to the center is large when running, as seen in Fig. 3.12. Although less affected when walking, it is still a larger deviation than desired.

4.3 Testing and results

The first tests conducted were with a damping elastic foam placed in two configurations according to Fig. 4.1, referred to as configuration 1 and 2. The resulting ISLA trace map for each configuration is presented in Fig. 4.2-4.4, along with the largest coordinate differences in Table 4.2. While testing the case for running, configuration 3 was used.

Figure 4.1: Damping configuration 1 and 2.

As can be seen from Fig. 4.2-4.4 and Table 4.2, there is a reduction in displacement for both the x- and y-coordinate. For the first configuration, there is a 3.3% increase in the displacement of the x coordinate, but an 18.4% in the y coordinate. For the second configuration the decrease is 10.8% and 14.1% in the x and y coordinate, respectively. Even when running, there is a decrease from the original value with 19% in the x coordinate and 15% in the y coordinate. This clearly indicates that the movement is reduced and that the damping plays a part in reducing the disturbances exerted on the entire camera.

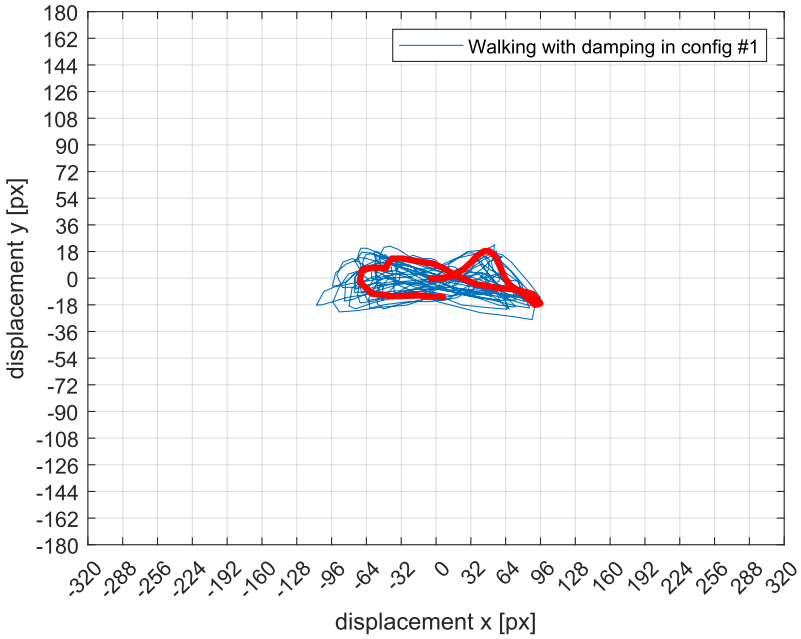

Figure 4.2: Walking with damping material placed according to configuration 1.

Figure 4.3: Walking with damping material placed according to configuration 2.

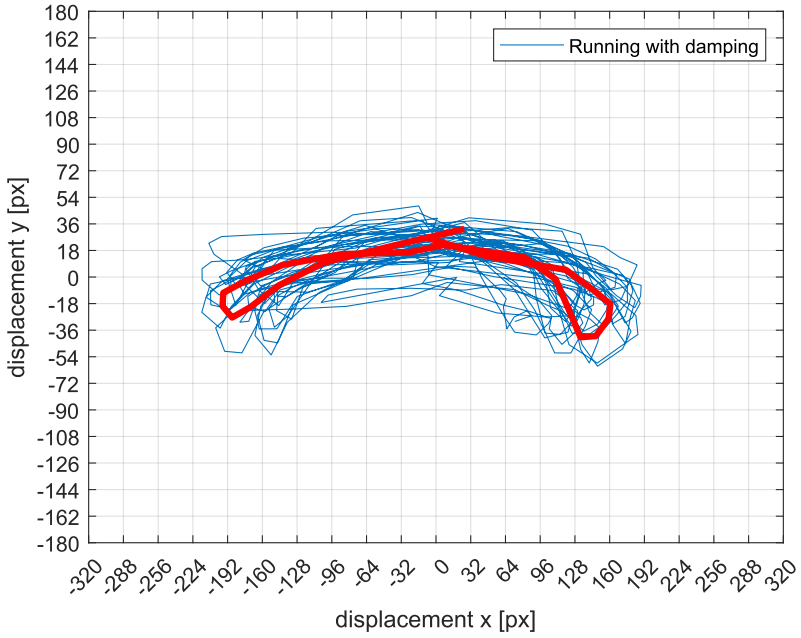

Figure 4.4: Running with damping in configuration 3.

Table 4.2: The deviations when testing the different damping configurations.

	$\lvert max(x) - min(x) \rvert$ [px]	$\lvert max(y) - min(y) \rvert$ [px]
Walking, no damping	199.18	62.00
Running, no damping	501.19	129.05
Configuration 1, walking	205.76	50.59
Configuration 2, walking	177.74	53.27
Configuration 3, running	404.78	108.62

There is a fourth configuration which is not included in Table 4.2, due to it only being used in combination with the active system. This configuration is placed in the same manner as Configuration 3, but utilizes a cast silicone piece instead, offering a higher stiffness than the PE foam.

The idea of using an IMU to compare gyroscope and accelerometer data was at first to see if there were any differences in rotational speeds (gyroscope) or accelerations when not using any damping materials vs. when using damping materials. By performing a Fourier transformation on the datasets, the frequencies of the sensors rotations and accelerations were calculated, as well as their amplitudes. See Table 4.3 and 4.4 for a comparison of walking without damping and walking with damping. See Table 4.5 and Table 4.6 for a comparison between the amplitudes for running without and with damping, respectively. The magnitude described is the maximum of that frequency and sensor parameter. To get the most out of the recorded signals, the energy spectral density of the base frequency and first four harmonics were compared to each other in the different cases, using Parseval's Theorem [46].

For a more in-depth analysis of the data gathered, variation in the placement of the IMU can be done. In the configuration that the IMU used for data gathering is placed at the time of this thesis, it does not record any data regarding the movement of the ISLA.

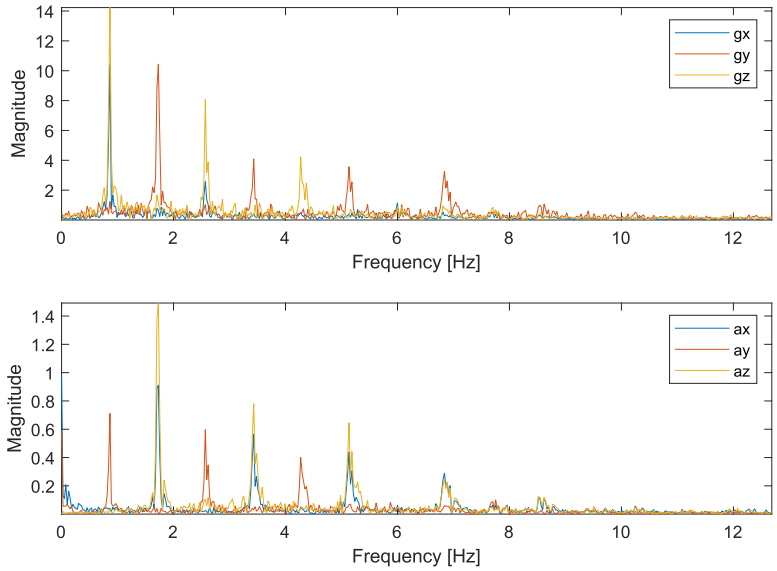

Figure 4.5: The frequency spectrum when walking without damping.

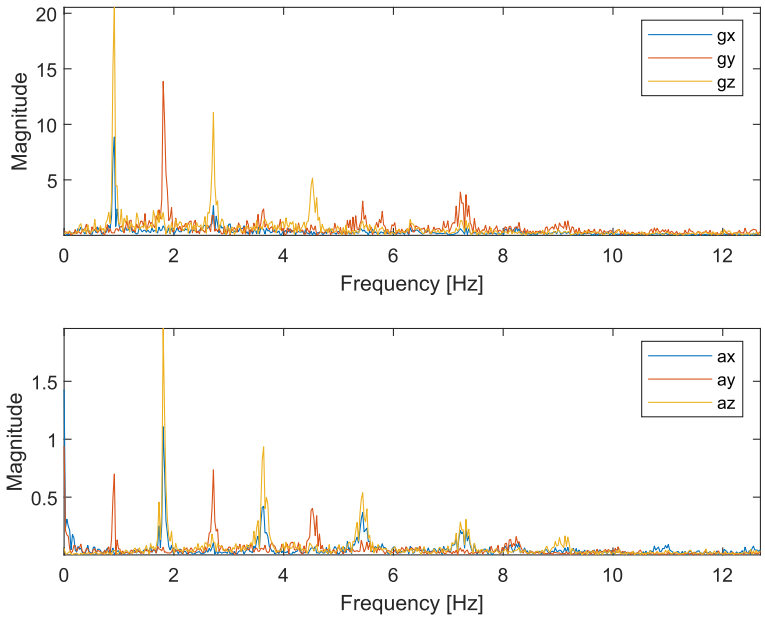

Figure 4.6: The frequency spectrum when walking with damping.

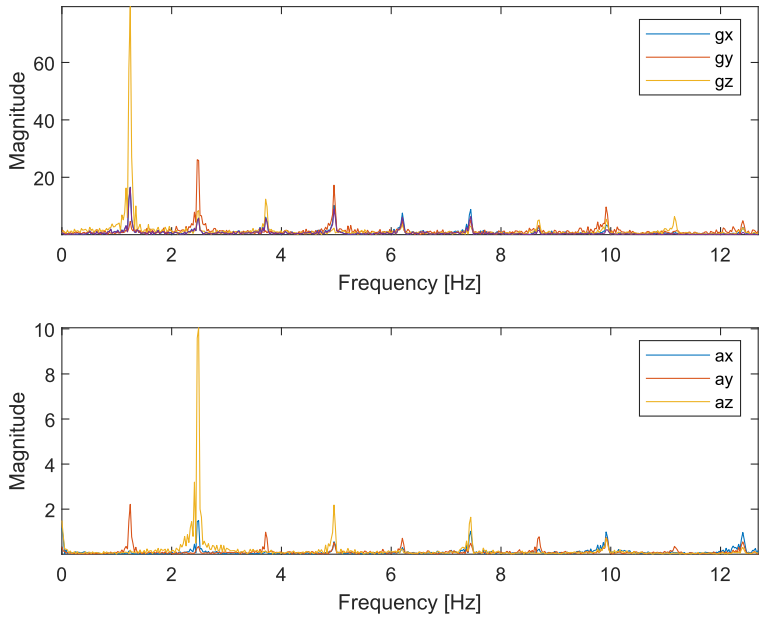

Figure 4.7: The frequency spectrum when running without damping.

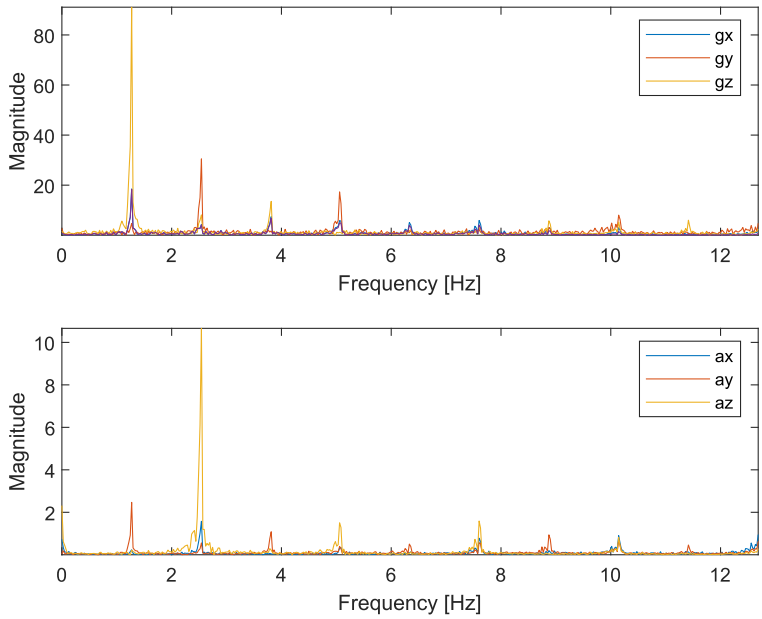

Figure 4.8: The frequency spectrum when running with damping.

Table 4.3: Frequency analysis data for the case of walking without any damping.

Walking, no damping	Magnitude@0.864 Hz	Energy Spectral Density
gx	10.33	47.4
gy	1.23	106.6
gz	14.24	133.7
ax	0.042	1.24
ay	0.71	0.61
az	0.036	2.1

Table 4.4: Frequency analysis data for the case of walking with damping.

Walking, damping	Magnitude@0.915 Hz	Energy Spectral Density
gx	8.82	51.4
gy	0.23	165.4
gz	20.536	300.1
ax	0.0022	1.62
ay	0.7	1.06
az	0.04	2.9

Table 4.5: Frequency analysis data for the case of running without any damping.

Running, no damping	Magnitude@1.255 Hz	Energy Spectral Density
gx	16.36	330.3
gy	4.63	763
gz	79.46	3078
ax	0.1389	4.2343
ay	2.2142	4.5277
az	0.1799	60.132

Table 4.6: Frequency analysis data for the case of running with configuration 3.

Running, damping	Magnitude @1.255 Hz	Energy Spectral Density
gx	18.496	266.7
gy	4.7047	709.4
gz	91.086	2943
ax	0.2347	3.1
ay	2.4689	4.6
az	0.2201	49.7

In Fig. 4.7 and 4.8, the frequency spectrum which the tabulated data is taken from, is displayed. Comparing this with the trace data presented in Table 4.2, there is a discrepancy in the measured quantities for the case of walking. The Spectral Densities in the comparison of running with and without damping indicates attenuation in some amplitudes for certain frequencies. The contribution is however marginal, which can also be concluded in the comparison of Fig. 3.12 and Fig. 4.4.

4.4 Combined system

In order to test how the stiffness of the damping element affects the performance, a silicone component was designed and cast, and represents configuration 4. This was done by aid of a colleague, with silicone of grade Shore 40A. Three tests each were performed for running and walking and the outcome did not differ much, but still improved the displacement in the y-coordinate. The combined system, i.e. both damping and control, is presented in Fig. 4.9 for the case of running. When running, the displacement in the y-coordinate without any damping elements and only control is 134.7 px, as shown in Table 3.6. When running with control and damping, the displacement is reduced to 71.6 px, a decrease of 48%. Thus, altering the stiffness of the passive MIS component by using a silicone casting instead of foam reduces the vertical displacement far more than previous materials used.

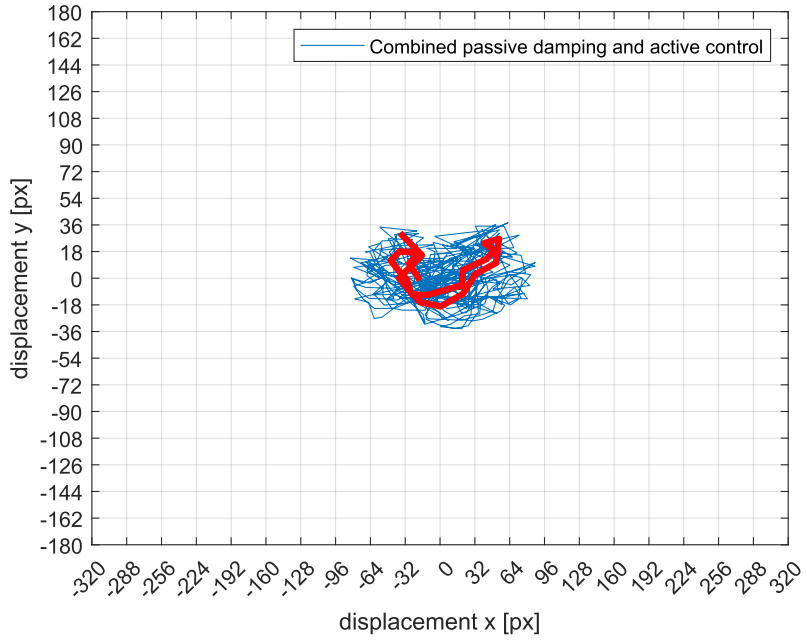

Figure 4.9: The trace map for the combined system.

The collected IMU data in itself does not point to any improvements. However, the

energy density of the spectrum for the damped cases suggests that some attenuation of the disturbances is present, as a decrease can be interpreted as the signal intensity being lower for that particular case. This can be seen when comparing Tab. 4.5 and 4.6. These types of graphs can be utilized in calculating the optimal material for damping, by providing the frequency of a gait cycle. This in turn provides the force acting on an object at a time instant t according to Eq. (2.13). Other quantities needed are in that case the objects mass, acceleration at time t and the displacement of the object at time t, all of which can be found by further developing the script presented in Appendix A.

Although the magnitude of the vibrations doesn't decrease between the cases, the damping material does have an impact on the cameras position at all times. In the normal case, the camera has some room for movement and this, by extension, introduces more ISLA movement. The spread in the y coordinate on the trace map is then increased and the image quality suffers. By adding an object that instead of using suspension to reduce vibrations caused by movement, there is currently a contrary desire to reduce the vibrations by reducing the suspension.

The effect of the different stabilization techniques are reviewed and discussed further in Chapter 6.

Chapter 5

Actuator Exploration

The actuator used in Chapter 3 is a 3-phase BLDC-motor which suits well for the application of controlling the angle of a ISLA. However, an issue that still remains is the size, actuation range and torque variation. As stated before, all components used to control the motor could be fit onto a single PCB in order for it to potentially fit into the camera instead of being placed on the outside of the BWC. The only part of the control system that is not possible to fit inside the camera is the actuator. Therefore it would be of interest to conceptualize an actuator that could fit, by adapting a different shape and actuating principle. Actuators commonly used in applications that have limited space are VCA:s, as described in Chapter 2.6. As this type of actuator also can be constructed in a limited angle span, it fits the application well. The important aspect is how the size affects the possibility to produce the torque and forces required to replace a BLDC-motor.

5.1 Concept

The concept which is explored in this chapter is a VCA, which is a single phase actuator that operates within a given span of angles. The idea for it is to better fit the application of controlling the ISLA direction with a main goal of it pointing forward at all times, independent of the wearers' body motion. Its function is based on electromagnetism like the actuator used in this thesis, meaning that a current flows through the coil which creates a magnetic field, moving the coil in a certain direction based on the magnitude and direction of current flow, when placed near stationary magnets.

The structure of a VCA varies, but the one proposed in this thesis is similar to a disk drive-VCA as described by Smith et. al [33], which is shown in Fig. 5.1 [47]. The disk drive-type VCA works by utilizing a pivot point which can be seen in Fig. 5.1, a voice coil, magnet(s) and upper (not shown) and lower fixture for the magnet(s). Granted, the

scale of these actuators are much larger than what is needed for the application of this exploratory study and simulations is performed in order to determine the forces produced with varying voltages and how this limits the possible size of the actuator.

Figure 5.1: A VCA used in disk drives. Image taken from SDM Magnetics [47]

5.2 System Specifications

The first step is deciding the initial dimensions for the VCA. The idea is that the ISLA is fastened to the pivot point and the VCA needs to be able to rotate within a specified span of angles, which in this case is a total of 50°. As can be seen in Fig. 5.1, the pivot points span of angles is limited by the width of the coil. Therefore, in order to include the set of angles, the arc on which the VCA moves needs to be long enough such that the middle of the coil can reach ±25°, as described in Fig. 5.2. With a coil width (and depth) of 10 mm, and a moment arm between the coil and pivot point of 3 mm, by simple trigonometry it is found that the geometry needs to accommodate an angle range of approximately ±85°. To simplify calculations and simulation, a rectangular shape of the fixture and magnets are adopted. This rectangular shape encompasses the specified angles, and its' dimensions are specified in Table 5.2.

As the ISLA is intended to be fastened to the pivot point, supporting structures carry the load of it. For the BLDCM used in Chapter 3, the force at start can be calculated by assuming that the force acts on the radius of the outrunner rotor. The radius of the airgap in the motor is approximated to be 14 mm (total radius 16 mm when including material) and the torque at start-up is 15.93 Nmm, yielding a force of roughly 1.1 N. The torque required to move the ISLA is decided by the weight of the ISLA, which is approximately 7 grams, resulting in a force $F_{base} = 0.0687$N, if calculating the force with 1 g, and a torque dependent on the moment arm. The force calculation serves as an approximation of the

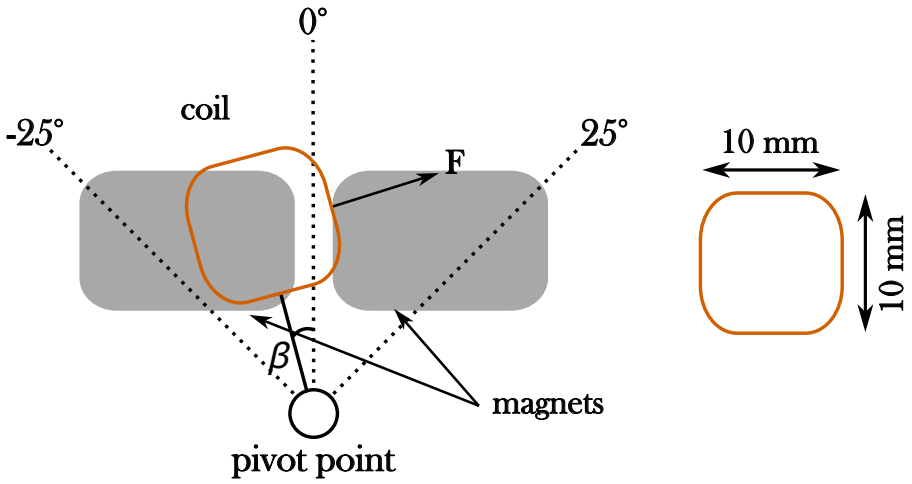

Figure 5.2: Illustration of the coil with magnets and coil width and length.

actual force by the ISLA. Comparison between the force generated by the BLDCM and the required force, the BLDCM outputs more than 10 times the required force.

The BLDCM has a start-up current to overcome the inertia of its own rotor, but the proposed actuator doesn't operate on the same principle as a BLDCM. Due to this, a start-up current is neither expected or accounted for in calculations and the current span in which the VCA operates is that of the BLDCM:s operating range, 6-26 mA. To calculate the number of turns needed for the coil, the resistance is decided to be the same as that of the BLDCM, R = 9.25Ω, which gives a maximum voltage of $0.026A * 9.25\Omega = 0.24V$. Then, the total length can be calculated using the given resistance, the copper resistivity $\rho = 1.68 * 10^-8$ [48] and the cross section of a 0.22 mm diameter copper wire [49]:

$$L_{total} = \frac{R * A_{coil}}{\rho} = \frac{9.25 * 3.8 * 10^{-8}}{1.68 * 10^{-8}} \approx 21m \tag{5.1}$$

As the coil has the width of 10 mm and depth of 10 mm, the mean turn length, l_{mean} is 40 mm and the number of turns can then be calculated:

$$N = \frac{L_{total}}{l_{mean}} = \frac{21}{0.04} = 525 \tag{5.2}$$

using Eq. 2.16 for N = 525 and assuming the flux density to be as high as B = 0.5T, the force produced by the coil can be calculated and verified (with $F_{base} = 0.0687$) [49]:

$$F = BiLN = 0.5 * 0.026 * 0.01 * 525 = 0.06825. \tag{5.3}$$

The current density in this case can be calculated as follows:

$$J_{coil} = \frac{i}{A_{coil}} = \frac{0.026A}{0.038mm^2} = 0.684\frac{A}{mm^2} \tag{5.4}$$

Which indicates there will be no larger issues with coil temperature, but it is important to keep in mind in the case of increased current. With a coil height, h_{coil} of 3 mm, the coil width can now be approximated [50]:

$$w_{coil} = d_{coil}^2 * \frac{N}{h_{coil}} = 0.00022^2 * \frac{525}{0.003} = 8.25mm \tag{5.5}$$

This width is on each side of the coil, resulting in a too large coil for the specified actuator. This means that the number of turns needs to be reduced, and a higher voltage needs to be applied. In Table 5.1, the number of turns are varied, and the corresponding coil cross-sectional width (c_{csw}), resistance (R_c), maximum current (I_{max}) and current density (J_{max}) are presented. The cross-section of the wire used is the same as before, d = 0.22 mm and the fill factor is 78.5% ($\frac{\pi}{4}$) due to the circular cross-section.

Table 5.1: Parameters depending on the number of turns.

N	c_{csw} [mm]	R_c [Ω]	I_{max} [A]	$J_{max}[A/mm^2]$
525	8.47	9.28	0.4	10.49
300	4.84	5.3	0.7	18.35
250	4.03	4.42	0.83	22.02
200	3.22	3.54	1.05	27.53
100	1.61	1.77	2.09	55.06
50	0.8	0.88	4.19	110.119

As can be seen, the maximum current no matter the number of turns exceed the current used from experimental testing (26 mA). This maximum current will output a force higher than needed and hence, current control will need to be implemented. There is of course freedom to vary any of the parameters i and N, depending on the desired characteristics of the actuator. Reducing the number of turns requires an increased current, which increases the power consumption. Although it would be desirable to use as low current as 26 mA, it simply isn't feasible to have 525 number of turns due to the size of the proposed VCA, as the width would exceed the size of the actuator itself. Hence, the current span is increased from the experiments performed in Chapter 3 and the number of turns decreased to 250. Ideally, the magnets are curved and follow the arc of the coil, but to simplify the simulations and initiate prototyping based on availability of PM material, the magnets used are rectangular and with a height of 1 mm, seen as the green rectangles in Fig. 5.3.

Table 5.2: Specifications on the coil based on magnet size

Moment arm [mm]	3
Coil length [mm]	10
Coil cross-sectional width [mm]	2.5
Coil cross-sectional height [mm]	3
Fixture length [mm]	20.5
Fixture width [mm]	18
Space between magnets [mm]	1
Current span [mA]	30-80
Number of turns	250
Required force [N]	0.07

The torque produced by the BLDC-motor within its' operating current can be calculated as follows, using K_T found in Eq. 3.2:

$$T_{26mA} = 0.03875 * 26mA \approx 1Nmm \tag{5.6}$$

The torque required by the VCA can be calculated using the approximated force produced by the weight of the ISLA and 1g of acceleration:

$$T_{base} = F_{base} * (r + \frac{l_{coil}}{2}) = 0.5496Nmm \tag{5.7}$$

Which is half the moment produced by the BLDC-motor at 26 mA. As stated previously, the current span needed to be increased in order to reduce the number of turns. The model upon which simulation is done is similar to the VCA presented in Fig. 5.1 but with two magnets, modelled similarly to Smith et al. [33] when simulating the actuator for limited angular motion. The specifications are presented in Table 5.2. In Fig. 5.3, the simulation model is shown (in meter scale). The coil length, which is the dimension into the graph, is 10 mm. The coil width, horizontal distance from the left edge of the left orange square to the right edge of the the right orange square is 10 mm. The top height of the top and bottom plate (dark gray) came through iterative testing, and is decided to be 2 mm. This is due to the plates providing stability and the thickness prevents them from getting fully saturated which would introduce magnetic leaks which can interfere with other devices within the actuators vicinity.

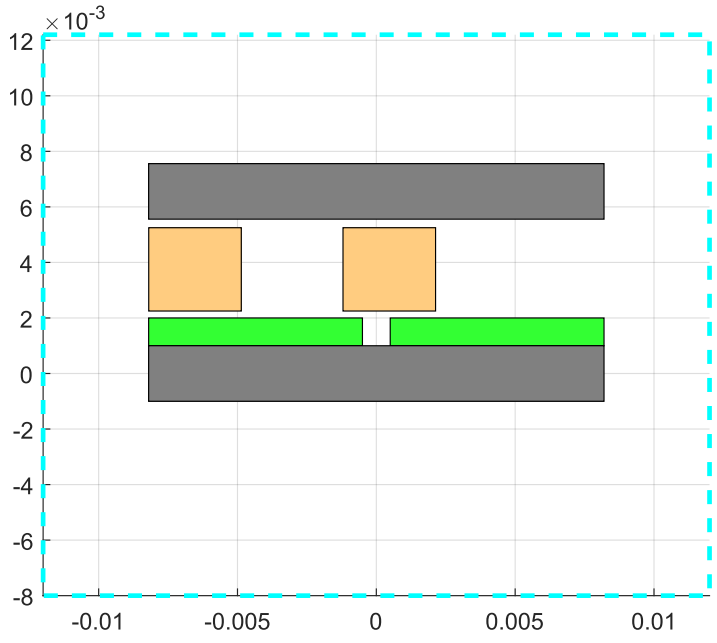

Figure 5.3: The model used in simulations.

Simulations

To illustrate the torque produced by the electromagnet, see Fig. 5.2, where there is a moment arm described by r, a Lorentz force F, and an angle β. The angle span needed to accommodate the coil is illustrated in Fig. 5.4

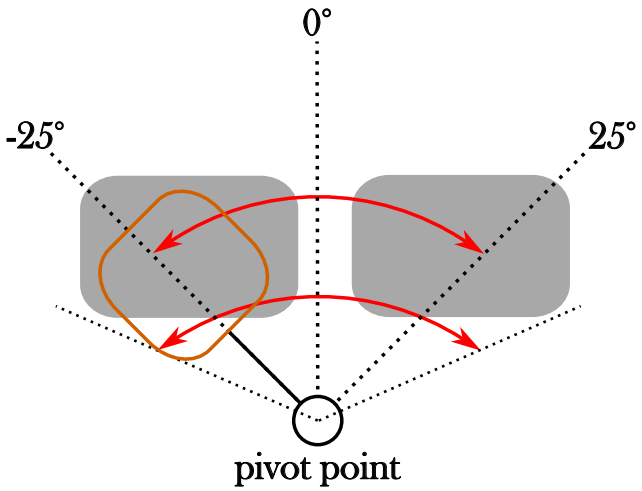

Figure 5.4: Two-dimensional illustration of the actual angle span needed for the coil

Assuming that the force acts at half the coil length, the torque about the pivot point can then be calculated as:

$$T_{pivot} = F(r + \frac{l_{coil}}{2})cos(\beta) \tag{5.8}$$

This formula can then be used to calculate the torque about the pivot point for any angle β within the given span of angles and for a varying current. The two key points in providing a constant torque is to have a constant moment arm and to control the current depending on the angle. As such, the applied current is a function of the coils angle relative to the pivot point.

In Fig. 5.5, the Lorentz force and flux linkage are plotted as functions of current and actuator position using FEMM, calculating the horizontal force and extracting the flux linkage, and the model used in simulations are entirely based on Table 5.2. When moving the coil within its' confined space, regardless of the current applied, the force output increases until reaching the middle, where it starts to decrease again. This means that to produce the necessary force, implementation of current control based on the coils position is necessary. As can be seen, all of the current levels except 30 mA can at certain points produce a force of the magnitude specified in Table 5.2. In Fig. 5.6 the torque calculated according to Eq. 5.2 is shown. As can be seen, for certain current levels and angular positions, the necessary torque is achieved.

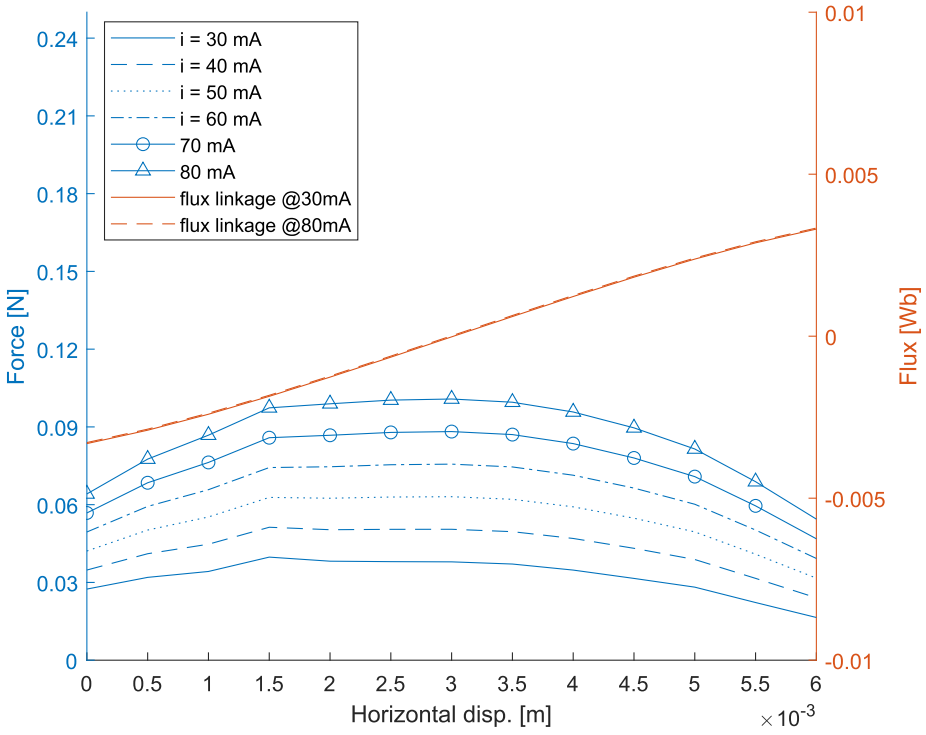

Figure 5.5: The force and flux linkage plotted as a function of position x.

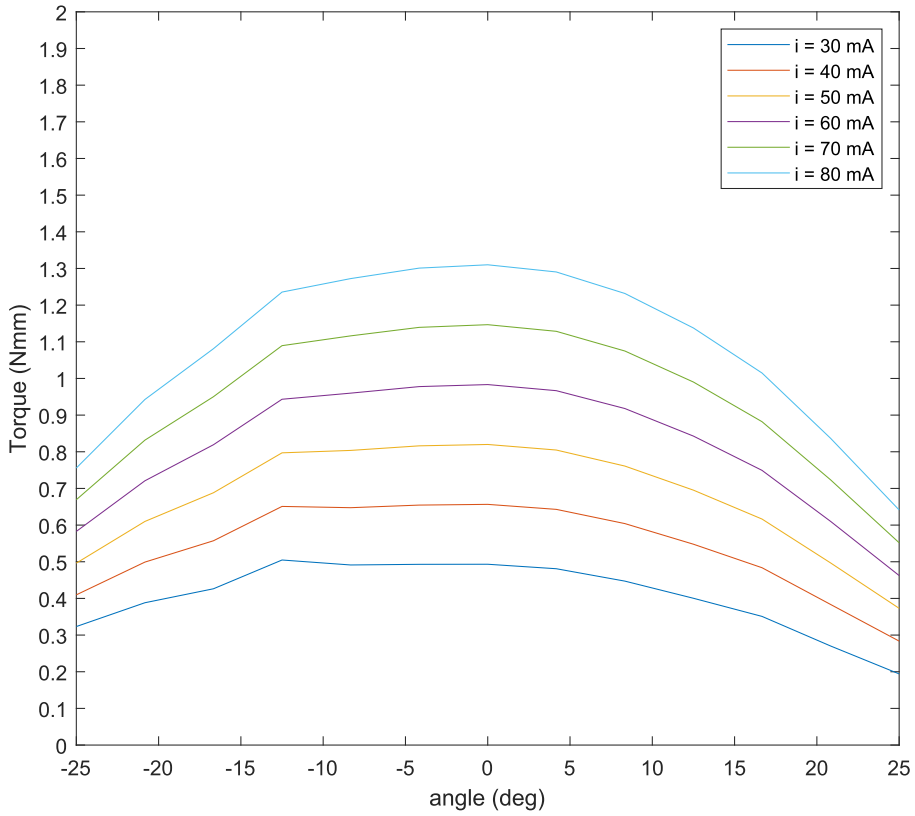

Figure 5.6: The torque as a function of the angle, calculated according to Eq. 5.4.

While the necessary torque is achieved at certain points throughout the movement, it is important to make sure that it always exceeds the required torque. Adding a load capability factor for the torque is a way to do this and another way is to explore the ideas experimentally by producing a set of coils to be tested. The required torque is calculated to be $\tilde{0}.55$ Nmm, and with a load capability factor of 10%, that is 1.1, the minimum torque to be achieved at all times throughout the movement is 0.6 Nmm. Taking this into account while studying Fig. 5.6, it can be seen that within the upper part of the current span, enough torque is produced for all angles with only 30 mA being too low. The characteristics shown in the graph indicate that the highest current in a control scenario is needed at the edges of the actuator, while steadily decreasing when approaching the zero position, i.e. when the coil pair is directly above their respective magnet. There is a tendency for the force to decrease as it reaches the opposite end point relative to the starting point. As can be seen, the required torque is achieved by modulating the current to be within the entire span of currents, i.e. 30-80 mA. Experimental work is a tool which can aid in understanding the slight drop-off in torque at the positive end of the angle span, as well as provide insightful information regarding a more exact current span to be used.

One could argue that a maximum of 60 mA is sufficient for providing the necessary torque for any of the angles specified, but experimentation would be the best evaluation tool for this.

The simulations performed using FEMM does not only include calculating force and flux linkage, but is a great tool for analyzing the flux density in the model and more importantly, in the air gap between the coil and the magnets. Referring back to Eq. 5.3, the flux density in the coil is estimated to be B = 0.5 T. In Fig. 5.7 the flux density is shown throughout the model, looking specifically at the flux density in the coil, it is concluded that B $\approx$ 0.4 T. This implies that F_{base} calculated in Eq. 5.3 is slightly lower. The coil is placed such that the highest force is achieved, with a current of 30 mA. As can be seen, the bottom plate is moderately saturated while the top plate is not near saturation. This is advantageous as it lessens the interference on other components within the actuators vicinity [51]. In Fig. 5.8, the flux density and Maxwell Stress tensor, which is used to calculate forces and torque in FEMM software [52], is shown. This is calculated for the entire width of the actuator, in the air gap beneath the coil (and not around the coil). B_n and B_t are the flux density in the normal and tangential direction, respectively. τ_n and τ_t are the Maxwell Stress tensor in normal and tangential direction, respectively. Above the magnets, the flux density is rather uniform, with a switch in the middle where there is a gap between the magnets. The highest Flux density is in the center of the voice coil actuator, corresponding well to the highest force being produced when the coil is centered over the magnets. The characteristics align with bi-directional force production dependent on the direction of current flow.

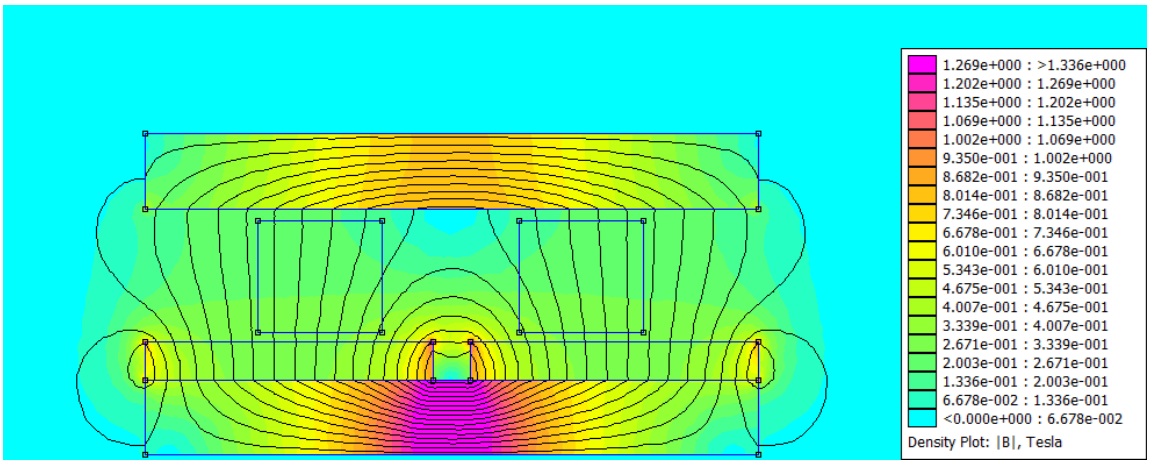

Figure 5.7: The flux density at the point of highest force.

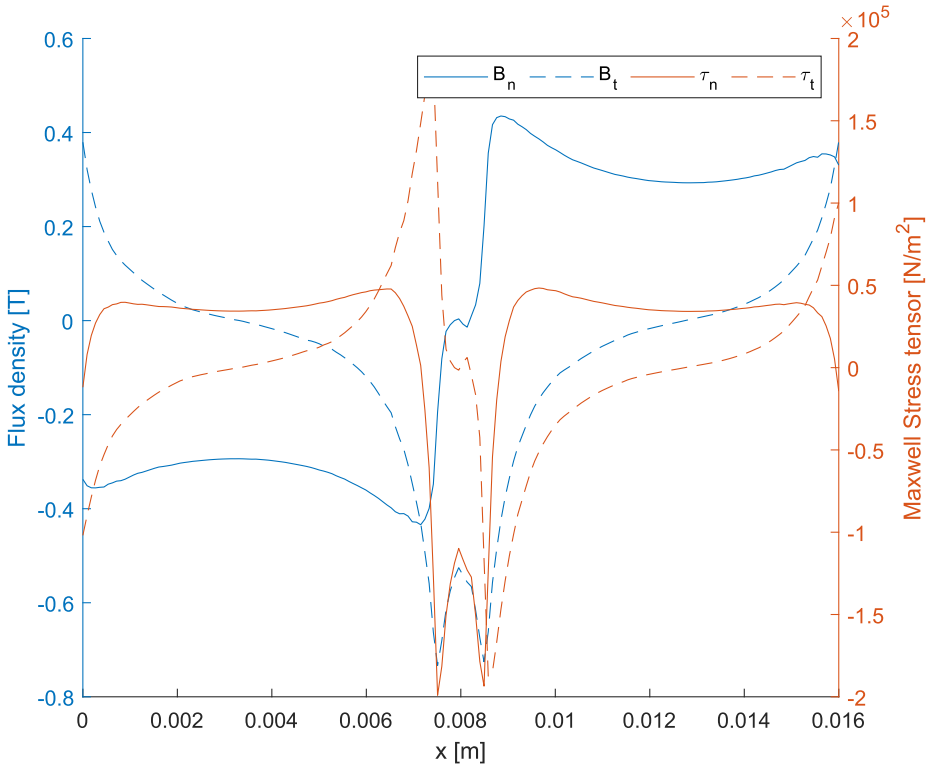

Figure 5.8: The flux density and stress tensor throughout in the air-gap between the coil and magnets.

5.3 CAD-based ideation

To aid in understanding the dimensions of the actuator and prepare for an actuator prototype, CAD is used to give a graphical representation. The idea is to be as close as possible to reality regarding sizing and placement. However, some dimensions such as the number of turns might not be definitive due to the adaptations made when "winding" a coil with CAD software. As the coil outer width, outer length and winding width are all specified in Section 5.2, they are used as the foundation for modeling. Everything is modeled around the coil, which is created first, and shown in Fig. 5.9.

The coil support mount partly holds the coil and partly connects the actuator to the pivot point. Its' design is shown in Fig. 5.10. As can be seen, it might be a tedious process to wind the coil with this configuration. As such, the coil holder should be divided into two parts and assembled after the coil is wound.

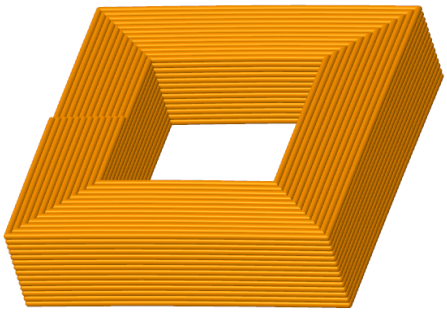

Figure 5.9: The coil used in modeling.

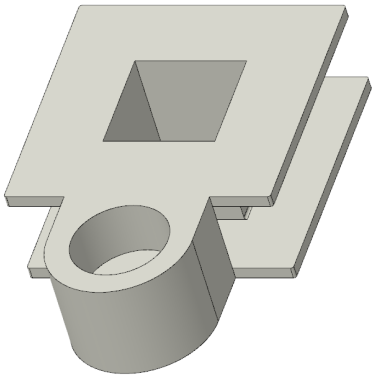

Figure 5.10: The coil holder.

The coil holder allows rotation by being fitted with a spherical roller bearing and connecting it to the bottom plate. The upper and bottom plates used to hold the actuator and magnets are then designed. These plates have two functions, partly to hold the actuator and partly to absorb the magnetic flux during actuation. Through simulation the thickness is found to be 2 mm and all other dimensions are fitted by the dimensions of the coil. In Fig. 5.11, the bottom and top plate are shown as well as the magnets used. The top and bottom plate are joined together by a bolt, creating a tension joint. The material used for the top and bottom plates is 1117 Steel with a relative permeability of $\mu = 1777$ [52] which, coupled with the specified thickness, has been shown through simulation to be high enough as it helps confine the magnetic field to the actuator. The magnets are neodymium magnets (N40 [52]), commonly used in a multitude of products such as electric motors, loudspeakers (voice coils), disk drives etc.

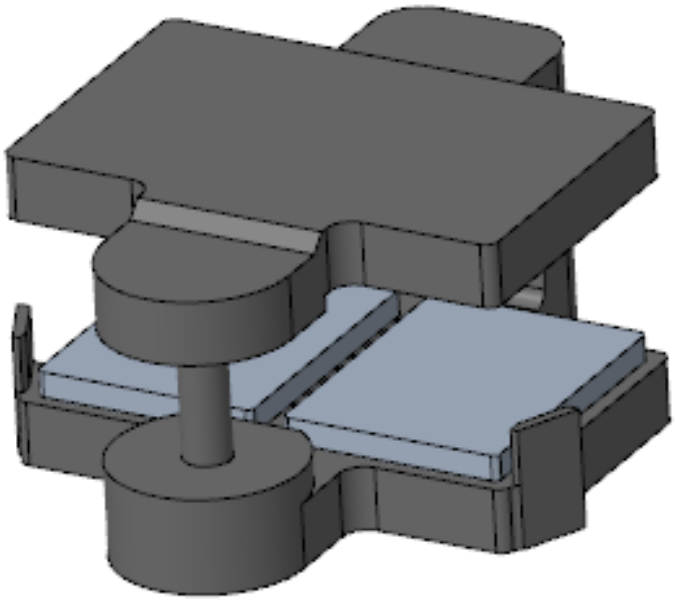

Figure 5.11: Top and bottom plates along with the magnets placed in the bottom plate.

The bearing used in this design has the outer diameter $d_o = 4$ mm, inner diameter $d_i = 1.5$ mm and height h = 2 mm. The fully assembled actuator as well as an exploded view are shown in Fig. 5.12.

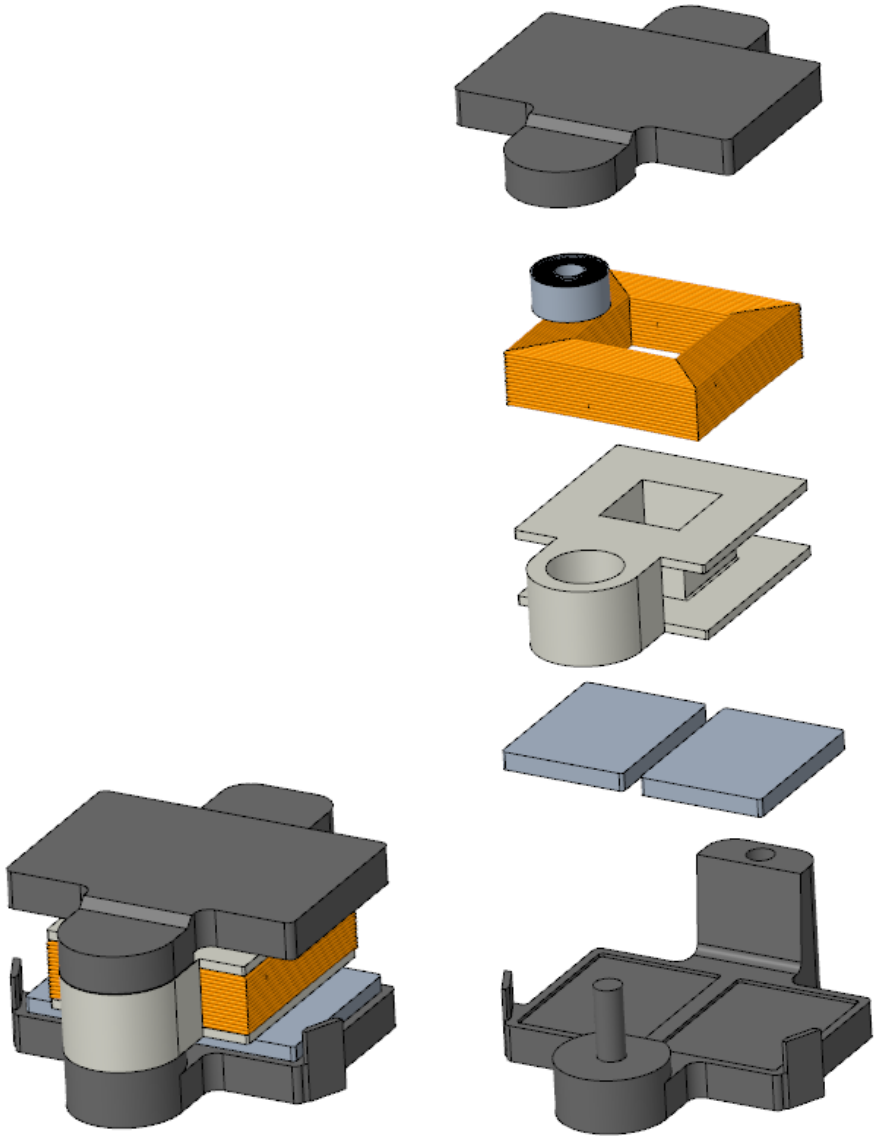

Figure 5.12: Left: The full actuator assembly. Right: the exploded view of the assembly.

In Fig. 5.13, the assembly is shown from the top view to illustrate which dimension is which. The length, l, of the actuator is 20.5 mm. The width, w, is 18 mm and the height is 9.75 mm. The size comparison with the BLDC-motor is discussed in Chapter 6.

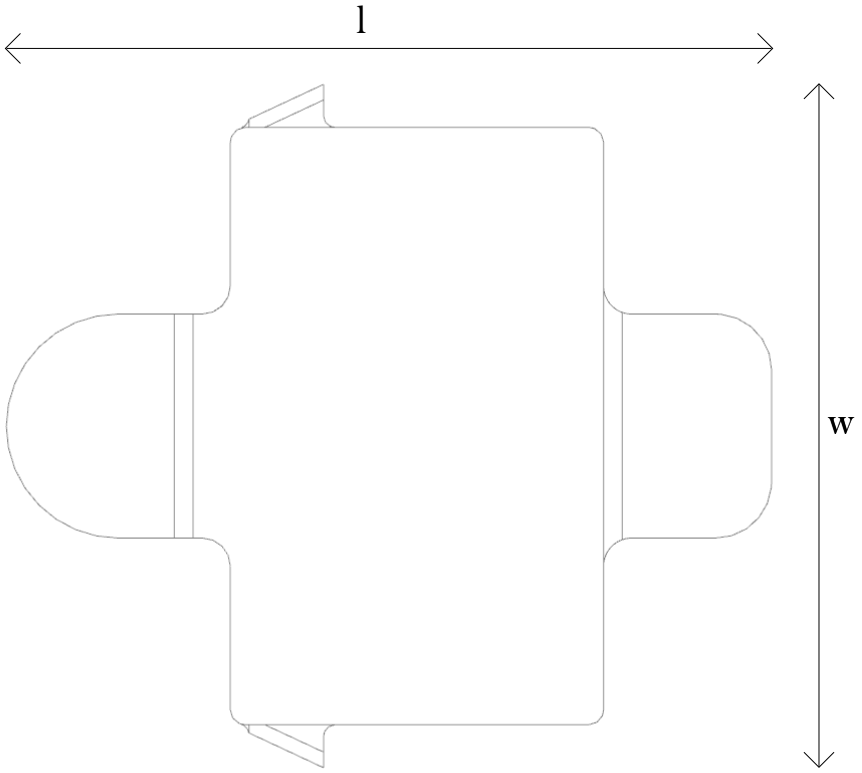

Figure 5.13: Top view of the actuator.

Chapter 6

Discussion

The purpose of this thesis was in part to investigate what characterizes the disturbances exerted on a BWC used in dynamic environments. With an understanding of the disturbances, one active and one passive MIS system is sought to be conceptualized and developed with the end product being a functioning prototype, demonstrating the ability to reduce disturbances. This involved selecting suitable components, evaluating power consumption, ensuring scalability of each component and the conceptualization of an actuator. Rigorous testing is done in order to properly evaluate the developed systems, with image analysis being the main evaluation tool. The image analysis method consisted of tracing the same object in the video feed for the system without control, with passive stabilization, with active stabilization and with the combined stabilization technique. A comparative image between the undamped system and fully damped and controlled system is presented in Fig. 6.1, and the deviations are listed in Table 6.1.

Table 6.1: Deviations in the x- and y-coordinates for the different systems.

	Deviation x [px]	Deviation y [px]	Change, x	Change, y
No MIS, 1.8 m/s	199.2	62	-	-
P MIS, 1.8 m/s	177.7	53.3	-10.8%	-14%
A MIS, 1.8 m/s	104.4	62.7	-47.6%	+1%
P+A MIS, 1.8 m/s	82.3	44	-58.7%	-29%
No MIS, 4 m/s	501.2	129	-	-
P MIS, 4 m/s	404.7	108.6	-19.2%	-15.8%
A MIS, 4 m/s	153.1	134.7	-69.5%	+4.4%
P+A MIS, 4 m/s	169.8	72	-66.1%	-44.2%

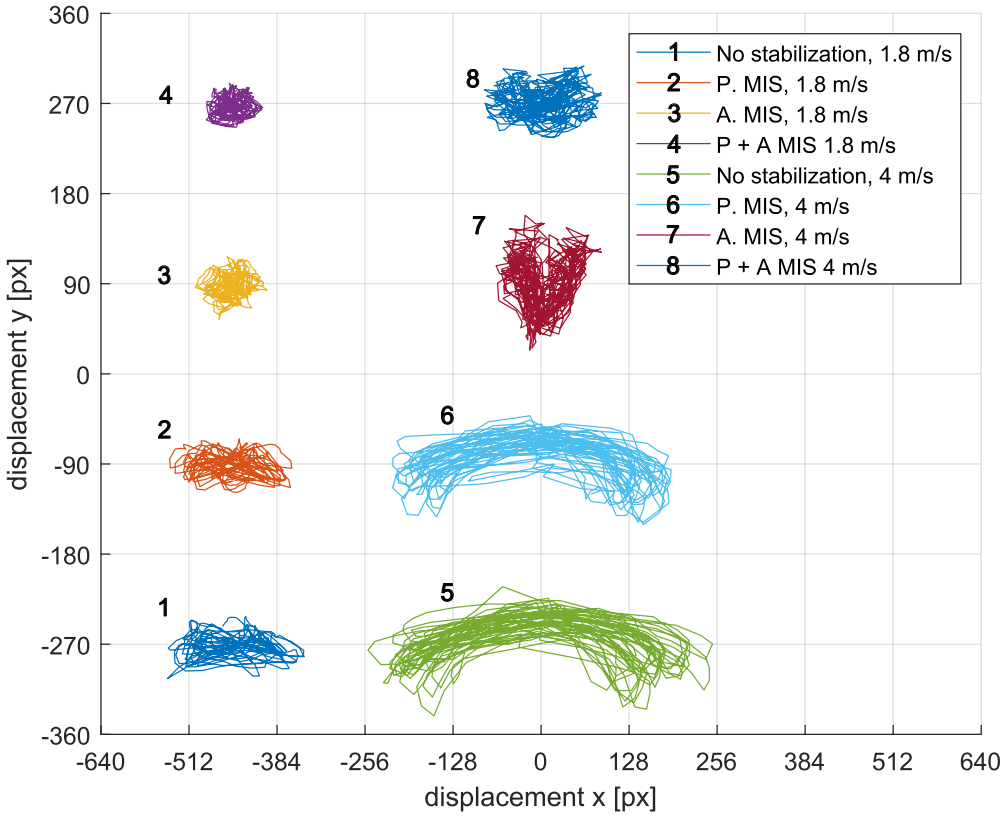

Figure 6.1: A comparative graph illustrating the differences when the system is undamped and uncontrolled and the opposite.

The passive MIS consisted of four different configurations, of which only two are shown here. The reason for this is that two configurations worked better than others, namely Configuration 4 and Configuration 3 as presented in Table 4.1. In the case of only passive MIS, configuration 3 is used and in the combined case, configuration 4 is used.

Active Mechanical Image Stabilization

In Chapter 3, a system to control the yaw-angle is constructed by starting at the specifications. The specifications were constructed by first evaluating the conclusions from previous work, described in Section 1.4. Regarding components, several time-saving decisions were made such as using a BLDC-motor which had been proven to work previously in [4] and using off-the-shelf solutions for the micro-controller and auxiliary sensors. This, as opposed to constructing an actuator from scratch and designing PCB:s, allowed more time to be spent on analyzing the function of the system, comparing and analyzing trace maps for different experimental MIS systems, and further exploring other solutions for stabilizing

the camera and ISLA. And as can be seen from the results of Chapter 3, the implemented system decreased the deviations of the lens forward direction, with a horizontal displacement reduction of 69.5% when running. Ideally, the tracing should only display deviations in the vertical axis. However, there are still indications of horizontal displacement for the active MIS, shown in Fig. 6.1. A possible cause for this is that the movement that the active system is in place to control isn't purely reciprocating. As a person is running, there occurs rotational movement of the upper body, such as swaying back and forth to each side, in a translational fashion. A purely rotational control system can't account for translational motion, thus leading to footage that still suffers from instability.

With all this in mind, the prototyped active MIS system reduces external disturbances at a low energy cost and for instance, a 10 minute period of active MIS consumes $E = P * t = 3.7V * 0.07A * \frac{10}{60}h = 0.043Wh$ or 11.2 mAh. No consideration for current control was taken regarding the system due to the low power consumption and the operating current being well below the specified current for the BLDC-motor. It would be of interest to explore this in the context of an alternative actuator, however. The current size of the solution is miniaturized but not minimized, as the possibility of constructing custom PCB:s to fit the micro-controller, sensors and drivers still exist. In Chapter 5, the possibility of constructing a smaller actuator than the BLDC-motor is explored, which would further the possibility of producing a completely integrated assembly.

Passive Mechanical Image Stabilization

The initial idea of utilizing passive damping elements in the prototype was that these dampers would reduce the angular velocity experienced by the camera when moving. Therefore, the first method for analyzing the results is to extract the angular velocity and linear accelerations from the IMU within the camera and investigate any differences. The aim of the work is to further analyze the kinematic model of the suspension (Section 2.4), but the introductory experiments on various P-MIS configurations showed a relatively small effect on stability when analysing the IMU data. The results of the IMU data analysis didn't point to any improvements, showing no signs of reduction in the aforementioned parameters. However, it is noticed that placing any material to be in contact with the backplate and camera whilst running had an effect, but not in the way previously thought, i.e. reducing the angular velocities. As there existed in the mounting solution which allowed the camera some space to move when mounted, placing an object between the backplate and camera introduced additional stiffness. From this point on, the more important analysis tool was the image analysis. From the trace graphs, there is a consistent reduction in the y-displacement of the tracked object and as such, the damping solution contributes to increased stability.

In the comparison of running, which is the worst case scenario, the damping provides a reduction of roughly 19% in the x-coordinate and 15% in the y-coordinate, seen in Fig. 6.1 and Table 6.1. This improvement comes from simply adding support material to make the camera have a firmer attachment and is easily implemented.

Combined System

The results of combining the two systems discussed in the previous section shows large reductions in both the x- and y-coordinate displacement. The reduction in movement is calculated between the best and worst trace coordinates, shown in Fig. 6.1. For walking, there is a 58.7% and 29% reduction in the x- and y-coordinate, respectively. For the case of running, there is a 66% and 44.5% reduction. There is a slight discrepancy in the use of the combined system and only using the active system, more specifically there is a 3% difference in x-coordinate reduction. This is probably due to variation in gait pattern during testing. Although the testing method was designed to eliminate as many variances as possible, there is still differences in ones running pattern. With that being said, the discrepancy is not a cause for concern regarding the validity of the results as both cases show improvements.

Actuator Concept

As the final part of this thesis, an alternative actuator was explored and conceptualized to address the scalability issue encountered with the actuator used in the prototype produced in Chapter 3. The prototype served as a foundation for this exploration, and the concept relies heavily on decisions made early on. As a starting point, it was decided that the actuator will be a VCA similar to the actuators used in disk drives, only smaller in size. The final size of the actuator is 20.5 x 18 x 9.75 mm (length, width, height), which results in a size reduction of 36%, 44% and 35% respectively, compared to the BLDC-motor. The size has been reduced and can provide the needed torque to replace the BLDC-motor, but no consideration has been taken as to how the ISLA should be fitted onto the actuator.

There is still work to be done regarding an alternative actuator, as a different configuration can prove to be better than the one proposed in this thesis. As the resistance of the coil was decided from the BLDC-motor, it governs the calculations that follows such as the number of turns and the general dimensions of the coil and by extension, the fixture. An increased current or an increased number of turns is needed to drive the actuator with the required force, but no further investigation into the exact span was done. To complement the simulations, experiments would need to be conducted in an effort to correctly specify

the exact span of current levels needed.

Chapter 7

Conclusions

This thesis begun by investigating the disturbances exerted on BWCs in two different use cases, namely walking and running. When the disturbances had been identified, development of a system of mechanical/electromechanical stabilization solutions to counter-act the disturbances was done. Further investigation into the scalability of the systems was done to conceptualize an alternative, smaller actuator to be used in the electromechanical part of the stabilization system.

The characteristics of the disturbances exerted on the camera when used are horizontal and vertical, caused by the biomechanics of the body. Swinging of the arms and the gait during running gives rise to a horizontally rotational motion. The gait also induces vertical motion, in a translational manner rather than rotational.

The disturbances were sought to be reduced and a two-part stabilization system was developed and evaluated. The first part of the stabilization system is an active system, constructed of an actuator, driver chip, micro-controller and two sensors; one to measure the angle of the actuator and one to measure the angle of the wearers body. This system greatly reduces the horizontal, rotational motion induced by running, by up to 69%, making the footage captured when running comparable to the footage captured when walking.

The second part of the system is a passive system, with the function of applying a more rigid connection of the camera housing to the mounting on the body. Different material stiffness were tested and it is concluded that the higher the stiffness, the better the result. This system reduces the vertical movement with up to 44%.

The final part of the thesis serves as a foundation for further work, and involved the conceptualization and simulations of an alternative actuator to the BLDC-motor used in the prototype. This actuator is, according to simulations, able to achieve the same forces as the BLDC-motor with a slightly higher current flow while being roughly 2/3 the size. This aids in reducing the size, i.e. enables scalability, of the active system.

The proposed MIS system in this thesis shows large improvements, reducing the disturbances to such an extent that it might be beneficial to implement EIS on top of it.

Future work

Multiple areas of improvement have been identified throughout the thesis. The first one is to delve deeper in the passive stabilization, by thoroughly experimenting with the materials used. This thesis showed that the right material can have a rather large impact in the stability of the recorded footage. An alternative to using materials to make the connection more rigid, an investigation into the connection to the mounting solution can be done.

The second area of improvement is the development and implementation of an alternative actuator. As was shown in this thesis, the performance of the BLDC-motor with a smaller actuator can be replicated in theory but is yet to be proven in reality. Here, design and experimentation is key. Peripheral devices such as a driver (such as an H-bridge) and micro-chip will be necessary to drive the actuator for the purpose of precise position control.

Another area were an effort is valuable is in the image analysis. In this thesis, the tracings used in the image analysis is done using commercial software intended for video editing. Developing a standalone object tracking software using e.g. Python might result in more precise results and allows for more data analysis due to its' sole purpose being image analysis.

Bibliography

[1] PBS NewsHour. Accessed 2024-12-05. URL: https://www.flickr.com/photos/newshour/7883965326/in/album-72157631241772396/.

[2] Merriam-Webster.com Dictionary. *biomechanics*. Accessed 2024-12-03. URL: https://www.merriam-webster.com/dictionary/biomechanics..

[3] . Bryngelsson and J. Gustafsson. "Image Stabilization for Body-Worn Cameras". MA thesis. Lunds Universitet, 2023.

[4] A. Bladh and J. Göransson. "Developing Stabilization System for Body-Worn Camera". MA thesis. Lunds Universitet, 2024.

[5] Merriam-Webster.com Dictionary. *Gimbal*. Accessed 2025-01-28. URL: https://www.merriam-webster.com/dictionary/gimbal.

[6] K. T. Ulrich and D. S. Eppinger. *Product Design and Development: Sixth Ed.* McGraw-Hill Education, 2016.

[7] Merriam-Webster.com Dictionary. *Stability*. Accessed 2024-12-03. URL: https://www.merriam-webster.com/dictionary/stability..

[8] J. Munafo et al. "The Rim and the Ancient Mariner: The Nautical Horizon Affects Postural Sway in Older Adults". In: *PLOS ONE* 11 (Dec. 2016), pp. 1–17. DOI: 10.1371/journal.pone.0166900. URL: https://doi.org/10.1371/journal.pone.0166900.

[9] L. Fortuna and G. Muscato. "A roll stabilization system for a monohull ship: modeling, identification, and adaptive control". In: *IEEE Transactions on Control Systems Technology, vol. 4, no. 1, pp. 18-28, doi: 10.1109/87.481763* (1996).

[10] Shuyan Xia et al. "Natural mechanism of superexcellent vibration isolation of the chicken neck". In: *Journal of Sound and Vibration* 594 (2025), p. 118649. ISSN: 0022-460X. DOI: https://doi.org/10.1016/j.jsv.2024.118649. URL: https://www.sciencedirect.com/science/article/pii/S0022460X24004115.

[11] Marcello Fusca, Paolo Perego, and Giuseppe Andreoni. "Method for Wearable Kinematic Gait Analysis Using a Harmonic Oscillator Applied to the Center of Mass". In: *Journal of Sensors* 2018.1 (2018), p. 4548396. DOI: https://doi.org/10.1155/2018/4548396. URL: https://onlinelibrary.wiley.com/doi/abs/10.1155/2018/4548396.

[12] ROHM Semiconductor. *Optical Image stabilization White Paper*. 2013.

[13] F. La Rosa et al. *Optical Image stabilization*. Accessed 2024-09-25. n.d. URL: https://www.st.com/resource/en/white_paper/ois_white_paper.pdf.

[14] Axis Communications. *Image Stabilization: Improving Camera Usability*. Accessed 2024-12-16. 2023. URL: https://www.axis.com/dam/public/f7/d0/f7/image-stabilization-en-US-423150.pdf.

[15] A. Bernardes and S. Violett. "Quaternion to Euler angles conversion: A direct, general and computationally efficient method". In: *PLoS ONE 17(11)* (2022).

[16] J. van Oosten. *Understanding Quaternions*. Retrieved 2024-12-02. URL: https://www.3dgep.com/understanding-quaternions/.

[17] Mecademic. *How to Use Quaternions in Industrial Robotics*. Retrieved 2024-12-02. URL: https://mecademic.com/insights/academic-tutorials/quaternions-in-industrial-robotics/.

[18] D. M. Henderson. *Euler Angles, Quaternions and Transformation matrices*. Tech. rep. Accessed 2024-11-21. NASA, 1977.

[19] A. Janota et al. "Improving the Precision and Speed of Euler Angles Computation from Low-Cost Rotation Sensor Data". In: *Sensors, 15* (2015).

[20] F. Wang, Z. Weng, and L. He. *Comprehensive Investigation on Active-Passive Hybrid Isolation and Tunable Dynamic Vibration Absorption*. Springer Singapore, 2018.

[21] Bing Z. et al. "The Vibration Isolation Technologies of Load in Aviation and Navigation". In: *International Journal of Multimedia and Ubiquitous Engineering* (2015).

[22] Epson. *Gyro Sensors*. Accessed 12/16/2024. URL: https://corporate.epson/en/technology/search-by-products/microdevice/gyro-sensor.html.

[23] V. M. N. Passaro et al. "Gyroscope Technology and Applications: A Review in the Industrial Perspective". In: *Sensors* (2017).

[24] Mojtaba Fazelinia, Saeed Ebadollahi, and Soheil Ganjefar. "Stochastic analysis of drift error of gyroscope in the single-axis attitude determination". In: *Measurement* 237 (2024), p. 115136. DOI: https://doi.org/10.1016/j.measurement.2024.115136. URL: https://www.sciencedirect.com/science/article/pii/S0263224124010212.

[25] I. Beavers. “The Case of the Misguided Gyro”. In: *Analog Dialogue 51-03* (2017).

[26] Inc. Omega Engineering. *How to measure acceleration?* Accessed 2024-09-17. 2024. URL: https://www.omega.com/en-us/resources/accelerometers.

[27] N. Ahmad, R. A. R. Ghazilla, and M. N. Nazirah M. Khairi. “Reviews on Various Inertial Measurement Unit (IMU) Sensor Applications”. In: *International Journal of Signal Processing Systems Vol. 1, No. 2* (2013).

[28] Physik Instrumente. *Gyroscopic Stabilization of a Hexapod 6-Axis Positioning Platform*. Accessed 2024-12-16. 2023. URL: https://www.pi-usa.us/en/tech-blog/gyroscopic-stabilization-of-a-hexapod.

[29] Hanifa Teimourian, Kamil Dimililer, and Fadi Al-Turjman. *Chapter Ten - Physics of stabilization and control for the Drone's quadrotors*. Ed. by Fadi Al-Turjman. Accessed 2024-12-16. Elsevier, 2020, pp. 189–205. DOI: https://doi.org/10.1016/B978-0-12-819972-5.00010-0. URL: https://www.sciencedirect.com/science/article/pii/B9780128199725000100.

[30] J. Zhao and Y. Yu. *Brushless DC Motor Fundamentals, Application Note*. Accessed 2024-12-04. URL: https://www.monolithicpower.com/media/document/Brushless_DC_Motor_Fundamentals.pdf.

[31] R. A. Roth II. “Performance and Modeling of Ultralinear Electrodynamic Actuator Systems”. MA thesis. University of Cincinatti, 2004.

[32] D. Collins. “How do rotary voice coil actuators work?” In: *Motion Control Tips* (2018). URL: https://www.motioncontroltips.com/how-do-rotary-voice-coil-actuators-work/.

[33] J. K. Smith, D. Graham, and J. Neasham. “Design and Optimisation of a Voice Coil Motor (VCM) with a Rotary Actuator for an Ultrasound Scanner”. In: *IEEE Transactions on Industrial Electronics 62(11):1-1* (2015). DOI: DOI:10.1109/TIE.2015.2449780.

[34] T.J.E. Miller. *Brushless Permanent-magnet and Reluctance Motor Drives*. Monographs in electrical and electronic engineering. Clarendon, 1993. URL: https://books.google.se/books?id=2AmxHwAACAAJ.

[35] Oncetop Motor Manufacture Co. Accessed 2024-10-7. URL: https://cdn.sparkfun.com/assets/e/b/2/8/3/OT-EM3215_DC_Brushless_Gimbal_Motor_3_Phase_Datasheet.pdf.

[36] Trinamic Motion control GmbH Co. Accessed 2024-12-09. URL: https://docs.sparkfun.com/SparkFun_Three_Phase_Motor_Driver-TMC6300/component_documentation/TMC6300.pdf.

[37] Raspberry Pi Ltd. Accessed 2024-12-11. URL: https://datasheets.raspberrypi.com/pico/pico-datasheet.pdf.

[38] ams Osram. Accessed 2024-12-11. URL: https://www.mouser.se/datasheet/2/588/AS5048_DS000298_4_00-2324531.pdf.

[39] TDK Corporation. Accessed 2024-12-11. URL: https://invensense.tdk.com/wp-content/uploads/2016/06/DS-000189-ICM-20948-v1.3.pdf.

[40] P. Dhaker. "Introduction to SPI interface". In: *Analog Dialogue, 52-09* (2018).

[41] T. Glad and L. Ljung. *Reglerteknik: Grundläggande teori, 4:e upplagan*. Studentlitteratur AB, Lund, 2006.

[42] M. Alaküla, P. Karlsson, and H. Bängtsson. *Power Electronics - Devices, Converters, Control and Applications*. course compendium, LTH, 2019, Accessed 2025-01-28.

[43] Y. Solbakken. *Vector Control for Dummies*. Accessed 2024-11-18. 2017. URL: https://www.switchcraft.org/learning/2016/12/16/vector-control-for-dummies.

[44] Y. Solbakken. *Space Vector PWM Intro*. Accessed 2024-11-21. 2017. URL: https://www.switchcraft.org/learning/2017/3/15/space-vector-pwm-intro.

[45] A. Skuric et al. "SimpleFOC: A Field Oriented Control (FOC) Library for Controlling Brushless Direct Current (BLDC) and Stepper Motors". In: *Journal of Open Source Software* 7.74 (2022), p. 4232. DOI: 10.21105/joss.04232. URL: https://doi.org/10.21105/joss.04232.

[46] M. Hassanzadeh and B. Shahrrava. "Linear version of Parseval's Theorem". In: *IEEE Access, vol. 10, pp. 27230-27241, doi: 10.1109/ACCESS.2022.3157736.* (2022).

[47] SDM Magnetics. Accessed 2024-12-11. URL: https://www.magnet-sdm.com/2019/11/04/voice-coil-motor-magnets/.

[48] *Electrical Resistivity and Conductivity*. Accessed 2024-12-22. URL: https://en.wikipedia.org/wiki/Electrical_resistivity_and_conductivity.

[49] *Electrical Engineering StackExchange*. Accessed 2024-12-22. URL: https://electronics.stackexchange.com/questions/350876/is-there-any-formula-to-get-number-of-windings-for-a-50w-voice-coil-of-a-speaker.

[50] *Coil winding technology*. Accessed 2024-12-22. URL: https://en.wikipedia.org/wiki/Coil_winding_technology.

[51] L. H. Dixon. *Magnetic Core Characteristics*. Accessed 2024-12-30. URL: https://www.ti.com/lit/ml/slup124/slup124.pdf.

[52] D. Meeker. *FEMM 4.2*. Material data found in Material Library. Accessed 2024-12-30. URL: https://www.femm.info/wiki/HomePage.

Appendix A: Conversion of IMU data and graph plotting

```
    \begin{verbatim}
%               z
%               |
%               |
%               |
%               |
%               |-------------y
%              /
%             /
%            /
%           /
%          x
% mass of object = 0.2 kg

clc;clear
readT = readtable("run_nomods1.csv");
l = length(readT(:,"gx").(1));
readT.t2 = rand(l);
tSerie = readT(:,"t");
t = zeros(l,0);
for i = 1:l
    t(i) = (tSerie.(1)(i)-tSerie.(1)(1))/12880000;
end
gxtab = readT(:,"gx");
gytab = readT(:,"gy");
gztab = readT(:,"gz");
gx = gxtab.(1);
gy = gytab.(1);
gz = gztab.(1);
% timeSeries = readT(:, "t2");
% t = timeSeries.(1);



axtab = readT(:,"ax");
aytab = readT(:,"ay");
```

```
aztab = readT(:,"az");
ax = axtab.(1);
ay = aytab.(1);
az = aztab.(1);

gx_off = -0.2899 + 4.8621e-05;
gy_off = -0.1120 + 3.3447e-05;
gz_off = -0.0856 + -2.9272e-05;
ax_off = -0.3994;
ay_off = -0.2008;
az_off = 3.5279e-4;
for i = 1:length(ax)
    ax(i) = 9.81*ax(i)*0.061/1000-ax_off;
    ay(i) = 9.81*ay(i)*0.061/1000-ay_off;
    az(i) = 9.81*az(i)*0.061/1000-9.806-az_off;

    gx(i) = pi*gx(i)*8.75/(1000*180);
    gy(i) = pi*gy(i)*8.75/(1000*180);
    gz(i) = pi*gz(i)*8.75/(1000*180);
    % gx(i) = gx(i)*8.75/1000-gx_off;
    % gy(i) = gy(i)*8.75/1000-gy_off; %in deg/s
    % gz(i) = gz(i)*8.75/1000-gz_off;
end

filtval = 32;
num = length(t);

arr_size = num/filtval;

gxavg = 0;
gyavg = 0;
gzavg = 0;
gxFilt = zeros(arr_size, 0);
gzFilt = zeros(arr_size, 0);
gyFilt = zeros(arr_size, 0);

axavg = 0;
ayavg = 0;
```

```
azavg = 0;
rollavg = 0;
pitchavg = 0;
axFilt = zeros(arr_size, 0);
ayFilt = zeros(arr_size, 0);
azFilt = zeros(arr_size, 0);
rollFilt = zeros(arr_size, 0);
pitchFilt = zeros(arr_size, 0);

ctr = 0;
tFilt = zeros(arr_size, 0);
for i = 1:length(gx)

    gxavg = gxavg + gx(i);
    gyavg = gyavg + gy(i);
    gzavg = gzavg + gz(i);
    axavg = axavg + ax(i);
    ayavg = ayavg + ay(i);
    azavg = azavg + az(i);
    pitchavg = pitchavg + atan(ax(i))/(sqrt(ay(i)*ay(i)+az(i)*az(i)))-0.2;
    rollavg = rollavg + atan(ay(i))/(sqrt(ax(i)*ax(i)+az(i)*az(i)));

    ctr = ctr + 1;
    if (ctr == filtval)
        gxavg = gxavg/filtval;
        gyavg = gyavg/filtval;
        gzavg = gzavg/filtval;
        axavg = axavg/filtval;
        ayavg = ayavg/filtval;
        azavg = azavg/filtval;
        rollavg = rollavg/filtval;
        gxFilt(i/filtval) = gxavg;
        gyFilt(i/filtval) = gyavg;
        gzFilt(i/filtval) = gzavg;
        axFilt(i/filtval) = axavg;
        ayFilt(i/filtval) = ayavg;
        azFilt(i/filtval) = azavg;
        rollFilt(i/filtval) = rollavg*180/pi+10;
```

```
        pitchFilt(i/filtval) = pitchavg*180/pi;
        tFilt(i/filtval) = t(i);
        ctr = 0;
        axavg = 0;
        ayavg = 0;
        azavg = 0;
        gxavg = 0;
        gyavg = 0;
        gzavg = 0;
        rollavg = 0;
    end
end

axmax = zeros(arr_size, 0);
axmin = zeros(arr_size, 0);

aymax = zeros(arr_size, 0);
aymin = zeros(arr_size, 0);

azmax = zeros(arr_size, 0);
azmin = zeros(arr_size, 0);

gxmax = zeros(arr_size, 0);
gxmin = zeros(arr_size, 0);

gymax = zeros(arr_size, 0);
gymin = zeros(arr_size, 0);

gzmax = zeros(arr_size, 0);
gzmin = zeros(arr_size, 0);

medax = zeros(arr_size, 0);
meday = zeros(arr_size, 0);
medaz = zeros(arr_size, 0);
medgx = zeros(arr_size, 0);
medgy = zeros(arr_size, 0);
medgz = zeros(arr_size, 0);
```

```
for i = 1:arr_size
    axmax(i) = max(axFilt);
    axmin(i) = min(axFilt);

    aymax(i) = max(ayFilt);
    aymin(i) = min(ayFilt);

    azmax(i) = max(azFilt);
    azmin(i) = min(azFilt);

    gxmax(i) = max(gxFilt);
    gxmin(i) = min(gxFilt);

    gymax(i) = max(gyFilt);
    gymin(i) = min(gyFilt);

    gzmax(i) = max(gzFilt);
    gzmin(i) = min(gzFilt);

    medax(i) = median(axFilt);
    meday(i) = median(ayFilt);
    medaz(i) = median(azFilt);
    medgx(i) = median(gxFilt);
    medgy(i) = median(gyFilt);
    medgz(i) = median(gzFilt);
end

%FILTERED PLOTS
% scale = 2;
%
% fig1 = figure(1);
% subplot(3,1,1);plot(tFilt, gxFilt);
% hold on
% plot(tFilt, medgx, 'Color', 'red');
% xlabel("time [s]")
% % ylabel("\omega [ \circ /s]") %deg/s
% ylabel("\omega [rad/s]") %rad/s
% % ylim([-5.1 5.1]); %rad/s
```

```
% % ylim([-300/scale 300/scale]); %deg/s
% xlim([0 max(tFilt)])
% legend("filtered g_x", "median g_x")
% %saveas(fig1, "gx_fast2.pdf")
%
% subplot(3,1,2);plot(tFilt, gyFilt)
% hold on
% plot(tFilt, medgy, 'Color', 'red');
% xlabel("time [s]")
% % ylabel("\omega [\circ /s]") %deg/s
% ylabel("\omega [rad/s]") %rad/s
% % ylim([-5.1 5.1]); %rad/s
% % ylim([-300/scale 300/scale]); %deg/s
% xlim([0 max(tFilt)])
% legend("filtered g_y", "median g_y")
% % saveas(fig2, "gy_fast2.pdf")
%
% subplot(3,1,3);plot(tFilt, gzFilt)
% hold on
% plot(tFilt, medgz, 'Color', 'red');
% xlabel("time [s]")
% ylabel("\omega [deg/s]") %deg/s
% %ylabel("\omega [rad/s]") %rad/s
% % ylim([-5.1 5.1]); %rad/s
% % ylim([-300/scale 300/scale]); %deg/s
% xlim([0 max(tFilt)])
% legend("filtered g_z", "median g_z")
% % % saveas(fig3, "gz_fast2.pdf")


% fig4 = figure(4);
% plot(tFilt, axFilt)
% hold on
% plot(tFilt, medax, 'Color', 'red');
% xlabel("time [s]")
% ylabel("\alpha [m/s^2]")
% %ylim([-7 7]);
% %xlim([0 max(tFilt)])
```

```
% legend("filtered \alpha_x", "median \alpha_x")
% % saveas(fig4, "ax_fast2.pdf")
%
%
% fig5 = figure(5);
% plot(tFilt, ayFilt)
% hold on
% plot(tFilt, meday, 'Color', 'red');
% xlabel("time [s]")
% ylabel("\alpha [m/s^2]")
% ylim([-7 7]);
% xlim([0 max(tFilt)])
% legend("filtered \alpha_y", "median \alpha_y")
% % % saveas(fig5, "ay_fast2.pdf")
%
% fig6 = figure(6);
% plot(tFilt, azFilt)
% hold on
% plot(tFilt, medaz, 'Color', 'red');
% hold on
% xlabel("time [s]")
% ylabel("\alpha [m/s^2]")
% xlim([0 max(tFilt)])
% legend("filtered \alpha_z", "median \alpha_z")
% % saveas(fig6, "az_fast2.pdf")
%
% gxmaxmin = [max(gxFilt), min(gxFilt)];
% gymaxmin = [max(gyFilt), min(gyFilt)];
% gzmaxmin = [max(gzFilt), min(gzFilt)];
% axmaxmin = [max(axFilt), min(axFilt)];
% aymaxmin = [max(ayFilt), min(ayFilt)];
% azmaxmin = [max(azFilt), min(azFilt)];
% disp("max/min values: ")
%
%
% fig7 = figure(7);
% plot(tFilt, pitchFilt)
% legend("estimated pitch angle");
```

```
% % % saveas(fig7, "angle_fast2.pdf")

% for j = 1:length(gxmaxmin)
%     disp(gxmaxmin(j))
% end
% for j = 1:length(gymaxmin)
%     disp(gymaxmin(j))
% end
% for j = 1:length(gzmaxmin)
%     disp(gzmaxmin(j))
% end
% for j = 1:length(axmaxmin)
%     disp(axmaxmin(j))
% end
% for j = 1:length(aymaxmin)
%     disp(aymaxmin(j))
% end
% for j = 1:length(azmaxmin)
%     disp(azmaxmin(j))
% end
```

Appendix B: Script for plotting the trace maps

```
clc;clear
f = ["run_ctrl","run_damping1","run_damping_ctrl","run_damping_ctrl2",
"run_everything","run_damping2","run_nomods2","run_spring_damping",
"walk_ctrl","walk_damping1","walk_damping2","walk_damping_ctrl",
"walk_everything","walk_nomods","walk_spring_damping"];
Filename = ["run_silicone_ctrl_new"];
meanx = zeros(length(f),1);
meany = zeros(length(f),1);
for i = 1:length(Filename)
    readT = readtable(Filename(i));
    l = length(readT(:,"Column1").(1));
    xtab = readT(:,"Column1");
    ytab = readT(:,"Column2");
    x = xtab.(1);
    y = ytab.(1);
    for j = 1:length(x)
        x(j) = x(j)*1920;
        y(j) = y(j)*1080;
    end
    meanx(i) = mean(x);
    meany(i) = mean(y);
    for k = 1:length(x)
        x(k) = x(k) - meanx(i);
        y(k) = y(k) - meany(i);
    end
    mag = 6;
    figure(1)
    hold on
    xlim([-1920/mag 1920/mag]);
    ylim([-1080/mag 1080/mag]);
    hold on
    grid on
    box on
    full = plot(x,y);
    period = plot(x(263:286),y(263:286));
    set(period,{'LineWidth'},{3},{'Color'}, {"red"})
    % disp("max and min: " + max(x) + " " + min(x))
```

```
    % disp("max and min: " + max(y) + " " + min(y))
    % disp("diff x: " + abs(max(x) - min(x)))
    % disp("diff y: " + abs(max(y) - min(y)))
end

% disp(max(x))
% disp(min(x))
% disp(max(y))
% disp(min(y))
% disp(abs(max(x)-min(x)))
% disp(abs(max(y)-min(y)))
legend("Combined passive damping and active control")
xticks(-1920/mag:32:1920/mag);
yticks(-1080/mag:18:1080/mag)
xlabel("displacement x [px]")
ylabel("displacement y [px]")
```

Appendix C: Calculations for the Fourier Transform of IMU data

```
clc
readT = readtable('walk_nomods1');
l = length(readT(:,'gx').(1));
readT.t2 = rand(l);
tSerie = readT(:,'t');
t = zeros(l,0);
for i = 1:l
    t(i) = (tSerie.(1)(i)-tSerie.(1)(1))/12880000;
end
gxtab = readT(:,'gx');
gytab = readT(:,'gy');
gztab = readT(:,'gz');
gx = gxtab.(1);
gy = gytab.(1);
gz = gztab.(1);
% timeSeries = readT(:, 't2');
% t = timeSeries.(1);
axtab = readT(:,'ax');
aytab = readT(:,'ay');
aztab = readT(:,'az');
ax = axtab.(1);
ay = aytab.(1);
az = aztab.(1);
for i = 1:length(ax)
    ax(i) = 9.81*ax(i)*0.061/1000;
    ay(i) = 9.81*ay(i)*0.061/1000;
    az(i) = 9.81*az(i)*0.061/1000-9.806;
    gx(i) = (gx(i)*8.75/1000+0.3994);
    gy(i) = (gy(i)*8.75/1000+0.2008);
    gz(i) = (gz(i)*8.75/1000);
end

windowSize = 50;
b = (1/windowSize)*ones(1,windowSize);
a = 1;
```

```
gxf = filter(b,a,gx);

hh=1:500;   % harmonic content
scrsz = get(0,'ScreenSize');
Fs = 833;   % Sampling frequency
Ts = 1/Fs;  % Sample time
L=l;        % length of signal
NFFT = 2^nextpow2(L); % Next power of 2 from length of y
f = Fs/2*linspace(0,1,NFFT/2);

y1=[gx gy gz];
Y1 = fft(y1,NFFT)/L;

% %figure(21); clf; set(gcf,'position',[5 50 scrsz(3)-10 600],'color',[1 1 1])
% %figure(21); %clf; set(gcf,'position',[5 50 scrsz(3)-10 600],'color',[1 1 1])
% figure(1)
% % hold on
% %subplot(3,1,1); plot(t,gx,'color',[0.00 0.45 0.74]);
ylabel('Rotational velocity, \omega [deg/s]'); axis tight
% % %legend('gx')
% % %hold on; plot(t,gxf,':','color',[0.00 0.45 0.74],'linewidth',1.5);
% % subplot(3,1,2); plot(t,gy,'color',[0.85 0.33 0.10]);
ylabel('Rotational velocity, \omega [deg/s]'); axis tight
% % legend('gy')
% % subplot(3,1,3); plot(t,gz,'color',[0.93 0.69 0.13]);
ylabel('Rotational velocity, \omega [deg/s]'); axis tight
% % legend('gz')
% % subplot(4,1,4); plot(f(hh),2*abs(Y1(hh,:))); axis tight
% subplot(2,1,1); plot(f(hh),2*abs(Y1(hh,:))); axis tight
% xlabel('Time [s]')
% legend('gx', 'gy', 'gz')
% % set(gca,'yscale','log')
%
% Yg = fft(y1)/L;
% rms_time = sqrt(mean(gz.^2));
% rms_fft = sqrt(sum(abs(Yg(:,3)).^2));
%
%
```

```
%
%
% % energy_t = sum(gx.^2)/L
% % energy_f = sum(abs(Yg(:,1)).^2)
%
% y2=[ax ay az];
% Y2 = fft(y2,NFFT)/L;
% hold on
% % figure(22); clf; set(gcf,'position',[5 50 scrsz(3)-10 600],'color',[1 1 1])
% % subplot(3,1,1); plot(t,ax,'color',[0.00 0.45 0.74]);
ylabel('Acceleration, \alpha [m/s^2]'); axis tight
% % legend('ax')
% % subplot(3,1,2); plot(t,ay,'color',[0.85 0.33 0.10]);
ylabel('Acceleration, \alpha [m/s^2]'); axis tight
% % legend('ay')
% % subplot(3,1,3); plot(t,az,'color',[0.93 0.69 0.13]);
ylabel('Acceleration, \alpha [m/s^2]'); axis tight
% %legend('az')
% % subplot(4,1,4); plot(f(hh),2*abs(Y2(hh,:))); axis tight
% subplot(2,1,2); plot(f(hh),2*abs(Y2(hh,:))); axis tight
% xlabel('Time [s]')
% legend('ax', 'ay', 'az')
% % set(gca,'yscale','log')
% ya = fft(y2)/L;
% sum(abs(Y1(hh,1)).^2)
% sum(abs(Y1(hh,2)).^2)
% sum(abs(Y1(hh,3)).^2)
% sum(abs(Y2(hh,1)).^2)
% sum(abs(Y2(hh,2)).^2)
% sum(abs(Y2(hh,3)).^2)
%
%
% % speed1 = zeros(1,500);
% % speed2 = zeros(1,500);
% % for i = 1:length(speed)
% %     speed1(i) = 1.8;
% %     speed2(i) = 4;
% % end
```

```
% % figure(3)
% % plot3(f(hh), speed1, 2*abs(Y(hh,2)))
% % hold on
% % plot3(f(hh), speed2, 2*abs(Y(hh,2)))
% % grid on
```